

## Supporting Information

### Forming chemisorbed single-molecule junctions through loss of stable carbocations

Jazmine Prana,<sup>a</sup> Luana Zagami,<sup>a</sup> Kelly Yan,<sup>a</sup> Daniel Hernangómez-Pérez,<sup>\*,b</sup> María Camarasa-Gómez,<sup>\*,c</sup> and Michael S. Inkpen<sup>\*,a</sup>

<sup>a</sup> Department of Chemistry, University of Southern California, Los Angeles, CA 90089, USA

<sup>b</sup> CIC nanoGUNE BRTA, Tolosa Hiribidea, 76, 20018 Donostia-San Sebastián, Spain

<sup>c</sup> Centro de Física de Materiales (CFM-MPC) CSIC-UPV/EHU, 20018 Donostia-San Sebastián, Spain

E-mail: [d.hernangomez@nanogune.eu](mailto:d.hernangomez@nanogune.eu), [maria.camarasa@ehu.eus](mailto:maria.camarasa@ehu.eus), [inkpen@usc.edu](mailto:inkpen@usc.edu)

## Contents

1. General Information	S2
2. Synthetic Details	S7
3. Additional Conductance Data	S10
4. Additional Computational Data	S25
5. NMR Spectra	S27
6. References	S30

## 1. General Information

### Synthesis and Characterization

Manipulations under a nitrogen atmosphere were carried out in oven-dried glassware using standard Schlenk line techniques. No special precautions were taken to exclude air or moisture during workup unless otherwise stated. Anhydrous dichloromethane ( $\text{CH}_2\text{Cl}_2$ ) and tetrahydrofuran (THF) were obtained by sparging with nitrogen and drying using a two-column solvent purification system packed with alumina (Pure Process Technologies, Nashua, NH, USA). Deionized water (initially  $18.2 \text{ M}\Omega$ ) was generated using an Arium® Mini Plus UV ultrapure water system (Sartorius AG, Goettingen, Germany). Deuterated solvents were purchased from Cambridge Isotope Laboratories, Inc., Cambridge Isotope Laboratories, Tewksbury, MA USA. Flash chromatography was performed using a Pure C-850 FlashPrep automated chromatography system and FlashPure EcoFlex flash cartridges (silica, irregular  $40\text{-}63 \mu\text{m}$  particle size,  $55\text{-}75 \text{\AA}$  pore size; BUCHI Corporation, New Castle, DE, USA), or by hand using Alfa Aesar silica gel 60 (215-400 mesh).  $^4\text{Bu}^1$  was prepared using established literature procedures. Other reaction solvents (sparged with nitrogen prior to use, where relevant), chemical reagents, and analyte molecules were commercially available and used without further purification. Reaction yields are unoptimized.

$^1\text{H}$  and  $^{13}\text{C}\{^1\text{H}\}$  NMR spectra were recorded at room temperature on Varian VNMRS 500 (500 MHz), VNMRS 600 (600 MHz), or Mercury 400 (400 MHz) NMR spectrometers.  $^1\text{H}$  NMR data recorded in  $\text{CDCl}_3$  and  $\text{CD}_2\text{Cl}_2$ , is referenced to residual internal  $\text{CHCl}_3$  ( $\delta$  7.26) and  $\text{CHDCl}_2$  ( $\delta$  5.32) solvent signals, respectively.<sup>2</sup>  $^{13}\text{C}\{^1\text{H}\}$  NMR data recorded in  $\text{CDCl}_3$  and  $\text{CD}_2\text{Cl}_2$  is referenced to internal  $\text{CDCl}_3$  ( $\delta$  77.16) and  $\text{CD}_2\text{Cl}_2$  ( $\delta$  53.84), respectively.<sup>2</sup> Mass spectrometry analyses were performed on a JEOL JMS-T2000GC AccuTOF GC-Alpha mass spectrometer (EI), at the Mass Spectrometry Lab, University of Illinois Urbana-Champaign.

### Scanning Tunneling Microscope-based Break Junction (STM-BJ)

#### *Experimental Details*

These details are reproduced here from a previous report, with only minor changes, for convenience.<sup>3</sup> STM-BJ measurements were performed using custom-built setups that have been described previously,<sup>4-6</sup> operated in ambient atmosphere or inside of a customized OMNI-Lab 4-port glovebox (Vacuum Atmospheres Company, Hawthorne, CA, USA). Hardware was controlled

and analyses were performed using custom software (written using IgorPro, Wavemetrics Inc., OR, USA). Experiments were conducted at room temperature under ambient conditions unless otherwise stated. Tip–substrate distances were controlled with sub-angstrom precision using a single-axis preloaded piezoelectric actuator (P-840.1, Physik Instrumente, MA, USA). Tunneling currents were measured using a DLPCA-200 variable gain low noise transimpedance current amplifier (FEMTO Messtechnik GmbH, Berlin, Germany). Applying a bias between the tip and substrate, conductance was measured as a function of tip–substrate displacement (at 40 kHz acquisition rate) as the tip was repeatedly pushed into the substrate to reach a conductance of  $>5 G_0$  (where  $G_0 = 2e^2/h$ ) and then retracted 5–10 nm (at 20 nm/s) to break the contact. The resulting conductance-distance traces were compiled into 1D conductance histograms (using 100 bins/decade along the conductance axis), or 2D conductance-distance histograms (using 100 bins/decade along the conductance axis and 1000 bins/nm along the displacement axis). Traces in 2D histograms were aligned such that displacement = 0 nm where  $G = 0.5 G_0$ . Color scales inset in 2D histograms are in count/1000 traces. Most probable conductance values for molecules studied here were obtained through Gaussian fits to their corresponding conductance peaks in 1D histograms.

STM tips were prepared from freshly cut Au wire ( $\varnothing = 0.25$  mm; 99.998%, Alfa Aesar, MA, USA or 99.999%, Beantown Chemical, NH, USA). Unless otherwise stated, substrates were prepared from evaporation of 100–200 nm Au (99.9985%, Alfa Aesar, or 99.999%, Angstrom Engineering Inc., ON, Canada) at a rate of  $\sim 1$  Å/s onto mechanically polished AFM/STM steel specimen discs (Ted Pella Inc., CA, USA) with a COVAP Physical Vapor Deposition System (Angstrom Engineering Inc.) used exclusively for metal evaporation. These gold substrates were UV-ozone cleaned (Probe and Surface Decontamination Standard System, Novascan Technologies, Inc., IA, USA) and used for measurements that same day. Measurements in propylene carbonate (PrC; Millipore-Sigma, anhydrous, 99.7%) were performed using STM tips coated with wax (Apiezon® Vacuum Sealing Wax W, M & I Materials Ltd, Manchester, UK) to leave only the apex area exposed; this serves to minimize background (non-tunneling) electrochemical currents.<sup>7</sup> For glovebox measurements, freshly cleaned substrates were brought through the ports by sparging rather than pump-fill cycles, to minimize possible contamination from the glovebox rotary vane vacuum pump (RV8, Edwards Vacuum, Burgess Hill, UK).

Template-stripped gold ( $\text{Au}^{\text{TS}}$ ) substrates were prepared through an adapted literature procedure.<sup>8,9</sup> Here, 200 nm of gold was evaporated at a rate of 1 Å/s onto a 4" Prime Grade <100> 1-10 Ohm cm<sup>-1</sup> 500-550 µm single side polished silicon wafer (Nova Electronic Materials, LLC, Texas, USA). Wafers were stored in clean room-packaged individual containers and only exposed to the laboratory environment immediately prior to loading in the metal evaporator. Glass tiles (10 mm × 10 mm × 3 mm) were employed as substrate supports. Prior to use, these tiles were cleaned by boiling in a 20% nitric acid bath for 10 min, rinsed with 18.2 MΩ·cm water ( $\text{H}_2\text{O}$ ), then dried and stored at 120°C. These substrates were affixed to a layer of metal on a silicon wafer support using Norland Optical Adhesive 61 (NOA 61) and cured for 900 s using a Traydex 18 Curing Oven (Norland Products, Jamesburg, NJ, USA). Immediately prior to use for STM-BJ measurements, individual  $\text{Au}^{\text{TS}}$  were cleaved from the silicon wafer using a razor blade, to reveal a clean, flat gold surface. Analyte solutions were localized on the substrate using a clean PTFE O-ring (0.07" fractional width, dash number 007, 9559K12; McMaster-Carr, Santa Fe Springs, CA, USA).

Glovebox STM-BJ experiments were typically started at single digit or sub-ppm  $\text{H}_2\text{O}$  and  $\text{O}_2$  concentrations, as measured by internal glove atmosphere sensors.  $\text{O}_2$  concentrations typically increase to 5-20 ppm during an experiment, as estimated by sensor readings upon re-initiation of air circulation. To minimize noise during data acquisition, circulation of the glovebox atmosphere was suspended, circulation valves were closed to isolate the catalyst, the vacuum pump was switched off, and the glovebox gloves were tied down to provide additional atmospheric stabilization. STM studies at 100°C were conducted using a custom-built resistive heating stage described previously.<sup>3</sup>

Directly before starting a solution measurement, ≥1,000 traces were collected to check the electrode surfaces were free from contamination. Analytes were typically studied as solutions (0.1-1 mM) tetradecane (TD; Millipore-Sigma, >99%), 1,3,5-trimethylbenzene (mes, Thermo Scientific Chemicals, 99%), squalane (SQ; Millipore-Sigma, 96%), 1-bromonaphthalene (BN; Millipore-Sigma, 97%), 1-chloronaphthalene (CN; Thermo Fisher Scientific, 85%, remainder 2-chloronaphthalene), PrC, or 1,2,4-trichlorobenzene (TCB; Millipore-Sigma, ≥99%). All solvents used in the glovebox were first sparged with nitrogen and dried over 3Å molecular sieves.<sup>10</sup> Molecular sieves were activated by heating for ≥3.5 h at 350°C in a muffle furnace (Thermolyne, Thermo Scientific, Asheville, NC, USA), and stored in a desiccator until use.

### *Conductance Noise Analysis*

We performed a conductance noise analysis for each measurement of **Tr**, **C<sub>7</sub>H<sub>7</sub>**, **Bn**, **H**, and **Me** using methods adapted from a previous report.<sup>5</sup> Each analysis first required us to identify the conductance region corresponding to transport through the molecular junction in individual conductance-displacement traces (the conductance step). To accomplish this, we fit Gaussian curves to the peaks in 1D histograms from each experiment, identifying the maximum and minimum conductance values characteristic of that molecular junction as the most probable conductance of each junction  $\pm 2\sigma$  (where  $\sigma$  is the standard deviation). The start of each conductance step was determined as the displacement after breaking the gold-gold point contact where the measured conductance fell below the maximum value. The end of each conductance step was determined as the displacement where the conductance rose above the minimum value from the instrumental noise floor. We considered that a conductance-displacement trace contained a step feature if the length of the step was greater than 0.1 nm and if the step was not highly sloped (highly sloped steps are indicative of the rapid exponential decay observed when a molecular junction is not formed). The slope of each conductance step was determined by taking the logarithm of the datapoints in the step and fitting it with a line. Junction formation probabilities, defined as the percentage of traces in each measurement that contained steps, are provided in **Table S3**. The logarithm of each extracted segment (the conductance step from each conductance-displacement trace), was then smoothed by averaging 11 neighboring points. For each trace we took the difference between the smooth and raw data for all the points in the step feature. These differences were then squared, the squared values were summed, and then this sum was normalized to the number of points in the segment to provide the noise parameter for that trace. The noise parameters for all traces with step features were then compiled into logarithmically binned noise histograms (using 10 bins/decade along the noise axis), and subsequently fit with Gaussian curves to provide the most probable noise values for each measurement (**Figure S14**).

### **Computational Details**

#### *Density Functional Calculations Details*

Our density functional theory (DFT) calculations were carried out using the FHI-aims package,<sup>11</sup> which implements the closed-shell Kohn-Sham DFT formalism. We employed the Perdew-Burke-Ernzerhof (PBE) non-empirical, generalized gradient approximation for the exchange-correlation

functional.<sup>12</sup> Scalar relativistic effects were incorporated via the zeroth-order regular approximation (ZORA) to account for relativistic corrections to the kinetic energy.<sup>13</sup> FHI-aims utilizes an optimized all-electron numeric atom-centered basis set. In this work, we adopted the so-called “light” computational settings, which correspond approximately to double-zeta basis set quality. The ground-state calculations were converged according to stringent self-consistent field (SCF) criteria: a particle density difference below  $10^{-5}$  electrons/ $\text{\AA}^3$  between consecutive iterations, a total energy change under  $10^{-7}$  eV, a variation in the sum of Kohn-Sham eigenvalues below  $10^{-4}$  eV, and a force convergence threshold of  $10^{-4}$  eV/ $\text{\AA}$ . All optimized geometries were obtained using the trust-radius-enhanced variant of the Broyden-Fletcher-Goldfarb-Shanno (BFGS) algorithm,<sup>11</sup> as implemented in FHI-aims. Structures were considered fully relaxed when all components of the residual atomic forces fell below the threshold of  $10^{-2}$  eV/ $\text{\AA}$ .

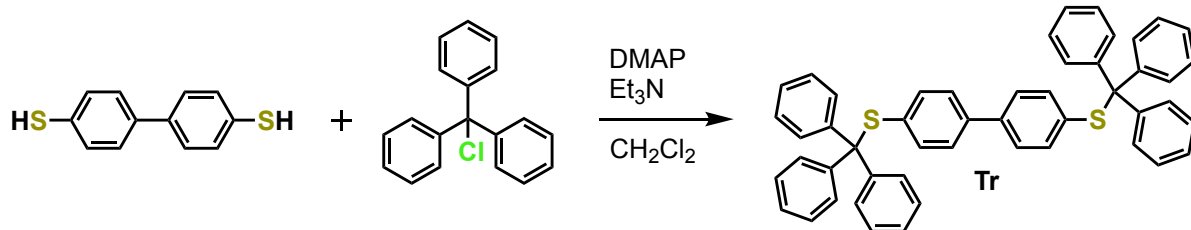
#### *Ab initio Quantum Transport Calculations Details*

The geometries of the model molecular junctions were determined through a well-established two-step procedure. First, the atomic positions of the molecule and the electrode apex were optimized using the methods and convergence criteria described above. This optimization was performed using pyramidal gold clusters comprising up to 11 gold atoms per tip. In the second step, the optimized molecular and tip geometries were kept fixed while additional gold layers were incorporated into the outer planes of the previously optimized electrode tips. This ensured proper screening of excess charge and accurate level alignment for subsequent quantum transport calculations.

The energy-dependent electronic transmission functions were computed within the linear response regime using the non-equilibrium Green’s function (NEGF) formalism, as implemented in the AITRANSS transport module.<sup>14–17</sup> Each junction electrode was modeled as a pyramidal face-centered cubic (FCC) cluster of 37 atoms, cut along the (111) direction with a nearest-neighbor distance of 2.88 Å. The electrode self-energies were approximated using an energy-independent (Markovian) local model, given by  $\Sigma(\mathbf{r}, \mathbf{r}') = i\eta(\mathbf{r})\delta(\mathbf{r} - \mathbf{r}')$ . The local absorption rate,  $\eta(\mathbf{r})$ , was fine-tuned to ensure that the electronic transmission remained stable under smooth, moderate variations in  $\eta(\mathbf{r})$  and was considered nonzero only within the outermost layers of the finite cluster.

## 2. Synthetic Details

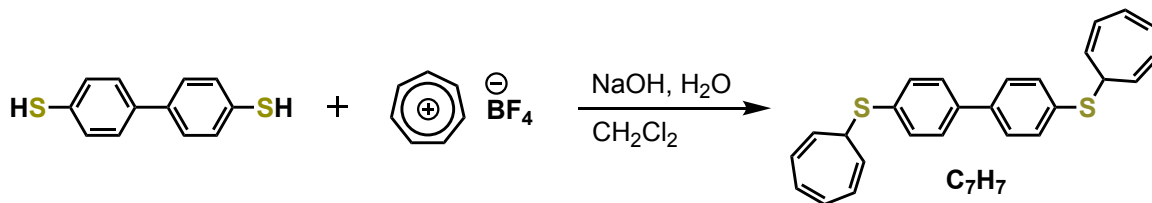
### *4,4'-Bis(tritylthio)-1,1'-biphenyl (Tr)*



This compound was prepared using an adapted literature method.<sup>18</sup>

Biphenyl-4,4'-dithiol (0.192 g, 0.879 mmol) and then triethylamine (0.25 mL, 1.80 mmol) was added to a stirred solution of trityl chloride (0.630 g, 2.26 mmol) and 4-dimethylaminopyridine (0.036 g, 0.295 mmol) in  $\text{CH}_2\text{Cl}_2$  (15 mL). The reaction flask was stoppered to minimize solvent evaporation. After 16 h, deionized water (~15 mL) was added to the green-yellow solution. The resulting mixture was extracted with  $\text{CH}_2\text{Cl}_2$  ( $3 \times \sim 20$  mL), whereby the combined organic layers were dried over  $\text{Na}_2\text{SO}_4$  and filtered before removing solvent by rotary evaporation. The crude product was preabsorbed onto Celite then purified using chromatography on a hexanes-packed  $\text{SiO}_2$  column, eluting with 0:1→1:1 v/v  $\text{CH}_2\text{Cl}_2$ -hexanes. Isolated material was further recrystallized by slow removal of  $\text{CH}_2\text{Cl}_2$  from a  $\text{CH}_2\text{Cl}_2$ -hexanes solution under vacuum to give **Tr** as a white crystalline solid (0.024 g, 4%).  $^1\text{H}$  NMR (500 MHz,  $\text{CD}_2\text{Cl}_2$ ):  $\delta$  (ppm) 7.41 (d,  $J = 7.5$  Hz, 12H, trityl- $H$ ), 7.22 (m, 18H, trityl- $H$ ), 7.14 (d,  $J = 8.6$  Hz, 4H, biphenyl- $H$ ), 6.96 (d,  $J = 8.5$  Hz, 4H, biphenyl- $H$ ).  $^{13}\text{C}\{\text{H}\}$  NMR (126 MHz,  $\text{CD}_2\text{Cl}_2$ ):  $\delta$  (ppm) 144.91 (trityl Ph,  $C_{\text{ispo}}$ ), 139.68 (biphenyl,  $CR_3$ ), 135.05 (biphenyl, C-H), 134.21 (biphenyl,  $CR_3$ ), 130.36 (trityl, C-H), 128.11 (trityl, C-H), 127.15 (trityl, C-H), 126.70 (biphenyl, C-H), 71.28 (trityl,  $C\text{Ph}_3$ ). HR-MS (EI+) m/z: 702.2396 ([M]<sup>+</sup> calc. for  $\text{C}_{50}\text{H}_{38}\text{S}_2$ : 702.2415).

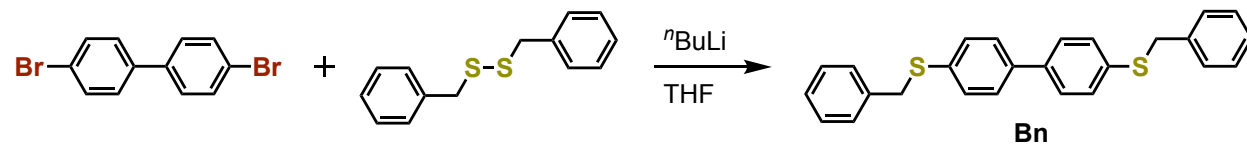
### *4,4'-Bis(cyclohepta-2,4,6-trien-1-ylthio)-1,1'-biphenyl (C<sub>7</sub>H<sub>7</sub>)*



This compound was prepared using an adapted literature method.<sup>19</sup>

A nitrogen-sparged 0.1 M solution of NaOH in deionized water (12.3 mL, 1.15 mmol) was added to a stirred solution of biphenyl-4,4'-dithiol (0.107 g, 0.490 mmol) in CH<sub>2</sub>Cl<sub>2</sub> (10 mL) under a N<sub>2</sub> atmosphere. Tropylium tetrafluoroborate (0.211 g, 1.19 mmol) was then added against a flow of N<sub>2</sub>. After vigorous stirring at room temperature overnight, the mixture was extracted into CH<sub>2</sub>Cl<sub>2</sub> (~25 mL) then washed with brine (3 × ~15 mL). The organic layer was dried over Na<sub>2</sub>SO<sub>4</sub> and filtered before removing solvent by rotary evaporation to give a yellow solid (0.162 g, 83%). <sup>1</sup>H NMR (400 MHz, CD<sub>2</sub>Cl<sub>2</sub>): δ (ppm) 7.49 (d, *J* = 7.2 Hz, 4H, biphenyl-*H*), 7.41 (d, *J* = 6.6 Hz, 4H, biphenyl-*H*), 6.64 (br s, 4H, C<sub>7</sub>H<sub>7</sub>-*H*), 6.29 (d, *J* = 9.3 Hz, 4H, C<sub>7</sub>H<sub>7</sub>-*H*), 5.58 (t, *J* = 8.4 Hz, 4H, C<sub>7</sub>H<sub>7</sub>-*H*), 3.99 (t, *J* = 6.8 Hz, 2H, CH-S). <sup>13</sup>C{<sup>1</sup>H} NMR (101 MHz, CD<sub>2</sub>Cl<sub>2</sub>): δ (ppm) 138.97 (biphenyl, CR<sub>3</sub>), 135.30 (biphenyl, CR<sub>3</sub>), 131.92 (C<sub>7</sub>H<sub>7</sub>, C-H), 131.56 (biphenyl, C-H), 127.52 (biphenyl, C-H), 127.38 (C<sub>7</sub>H<sub>7</sub>, C-H), 124.75 (C<sub>7</sub>H<sub>7</sub>, C-H), 46.10 (C<sub>7</sub>H<sub>7</sub>, C-S). HR-MS (EI<sup>+</sup>) m/z: 398.1168 ([M]<sup>+</sup> calc. for C<sub>26</sub>H<sub>22</sub>S<sub>2</sub>: 398.1163).

#### *4,4'-Bis(benzylthio)-1,1'-biphenyl (**Bn**)*

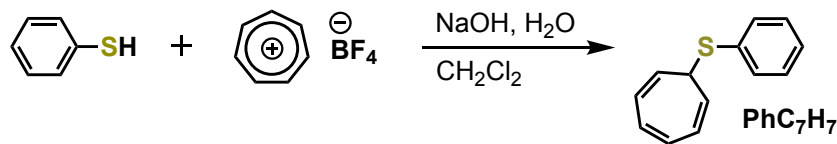


This compound was prepared using an adapted literature method.<sup>20</sup>

A solution of 1.6 M *n*-butyl lithium in hexanes (1.2 mL, 1.92 mmol) was added dropwise to a stirred solution of 4,4'-dibromobiphenyl (0.217 g, 0.696 mmol) in THF (6 mL) under a N<sub>2</sub> atmosphere at -78°C (dry ice/acetone bath). After 10 min, dibenzyl disulfide (0.681 g, 2.76 mmol) was added against a flow of N<sub>2</sub> and the mixture was allowed to warm to room temperature with stirring over 16 h. Deionized water (10 mL) was added to the resulting turbid orange solution to quench any unreacted organolithium species. The mixture was extracted into CH<sub>2</sub>Cl<sub>2</sub> (10 mL), whereby the organic layer was washed with brine (3 × ~10 mL), dried over MgSO<sub>4</sub>, and filtered before removing solvent by rotary evaporation. The crude product was preabsorbed onto Celite then purified using chromatography on a hexanes-packed SiO<sub>2</sub> column, eluting with hexanes. Isolated material was further recrystallized by slow removal of CH<sub>2</sub>Cl<sub>2</sub> from a CH<sub>2</sub>Cl<sub>2</sub>/hexanes solution under vacuum to give **Bn** as a white crystalline solid (0.017 g, 6%). Spectroscopic data is consistent with previous reports.<sup>20</sup> <sup>1</sup>H NMR (500 MHz, CD<sub>2</sub>Cl<sub>2</sub>): δ (ppm) 7.48 (d, *J* = 8.5 Hz, 4H, biphenyl-*H*), 7.35 (m, 8H, overlapping biphenyl-*H* and benzyl-*H*), 7.30 (m, 4H, benzyl-*H*), 7.24

(m, 2H, benzyl-*H*), 4.17 (s, 4H, *CH*<sub>2</sub>). <sup>13</sup>C{<sup>1</sup>H} NMR (126 MHz, CD<sub>2</sub>Cl<sub>2</sub>) δ (ppm) 138.52 (Ar, CR<sub>3</sub>), 137.96 (Ar, CR<sub>3</sub>), 136.18 (Ar, CR<sub>3</sub>), 130.12 (Ar, C-H), 129.20 (Ar, C-H), 128.88 (Ar, C-H), 127.59 (benzyl, C-H), 127.49 (biphenyl, C-H), 39.00 (*CH*<sub>2</sub>). HR-MS (EI+) m/z: 398.1167 ([M]<sup>+</sup> calc. for C<sub>26</sub>H<sub>22</sub>S<sub>2</sub>: 398.1163).

*(Cyclohepta-2,4,6-trien-1-ylthio)-phenyl (PhC<sub>7</sub>H<sub>7</sub>)*



This compound was prepared using an adapted literature method.<sup>19</sup>

A nitrogen-sparged 0.1 M solution of NaOH in deionized water (29 mL, 2.9 mmol) was added to a stirred solution of thiophenol (0.2 mL, 1.9 mmol) in CH<sub>2</sub>Cl<sub>2</sub> (4 mL) under a N<sub>2</sub> atmosphere. Tropylium tetrafluoroborate (0.522 g, 2.93 mmol) was then added against a flow of N<sub>2</sub>. After vigorous stirring at room temperature overnight, the mixture was extracted into CH<sub>2</sub>Cl<sub>2</sub> (~20 mL) then washed with brine (3 × ~15 mL). The organic layer was dried over Na<sub>2</sub>SO<sub>4</sub> and filtered before removing solvent by rotary evaporation to give a pale yellow oil (0.326 g, 84%). Spectroscopic data is consistent with previous reports.<sup>19</sup> <sup>1</sup>H NMR (600 MHz, CDCl<sub>3</sub>): δ (ppm) 7.38 (d, *J* = 8.0 Hz, 2H, Ph-*H*), 7.27 (t, *J* = 7.5 Hz, 2H, Ph-*H*), 7.21 (t, *J* = 7.3 Hz, 1H, Ph-*H*), 6.64 (br s, 2H, C<sub>7</sub>H<sub>7</sub>-*H*), 6.27 (d, *J* = 10.6 Hz, 2H, C<sub>7</sub>H<sub>7</sub>-*H*), 5.56 (t, *J* = 8.2 Hz, 2H, C<sub>7</sub>H<sub>7</sub>-*H*), 3.91 (t, *J* = 6.8 Hz, 1H, C<sub>7</sub>H<sub>7</sub>-*H*). <sup>13</sup>C{<sup>1</sup>H} NMR (151 MHz, CDCl<sub>3</sub>): δ (ppm) 135.55 (Ph, CR<sub>3</sub>), 131.68 (C-H), 131.20 (C-H), 128.95 (C-H), 126.99 (C-H), 126.84 (C-H), 124.70 (C-H), 45.92 (C<sub>7</sub>H<sub>7</sub>, C-S). HR-MS (EI+) m/z: 200.0655 ([M]<sup>+</sup> calc. for C<sub>13</sub>H<sub>12</sub>S: 200.0660).

### 3. Additional Conductance Data

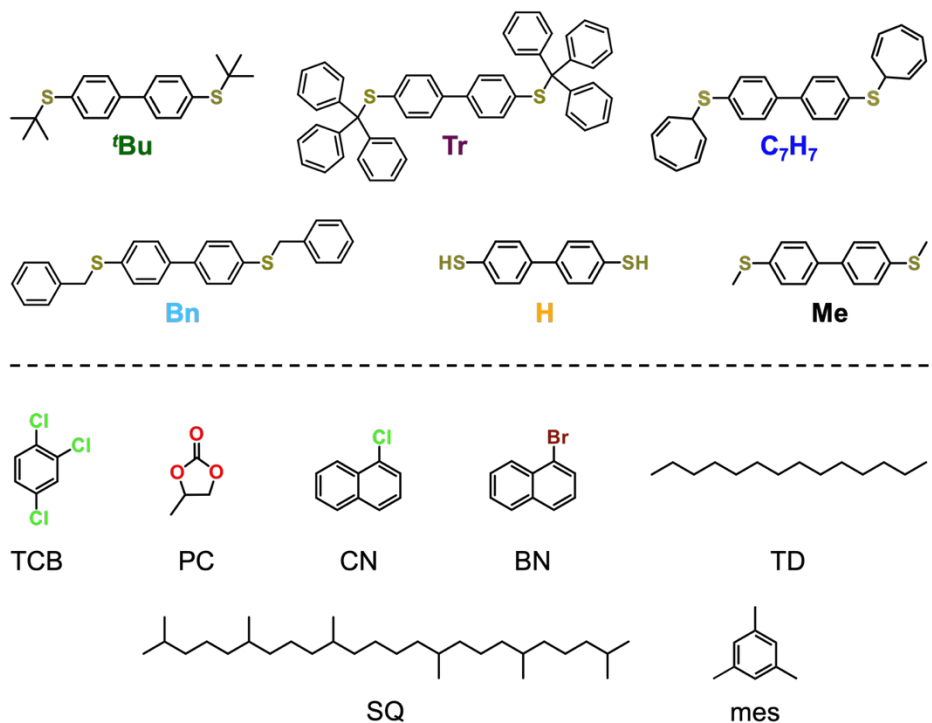


**Figure S1.** Molecular structures of all compounds (top) and solvents (bottom) used in this study.

*Conductance Measurements of  ${}^t\text{Bu}$*

**Table S1.** Conductance data from measurements of  ${}^t\text{Bu}$  in **Figures 2 and 3.**<sup>a</sup>

panel	geometry	conditions	V <sub>bias</sub> (V)	conductance (G <sub>0</sub> )	absolute area	%-C <sup>b</sup>
<b>2b,3a</b>	PP	TD	0.10	$1.08 \times 10^{-4}$	0.745	65.1
	PC <sup>c</sup>		(first)	$7.06 \times 10^{-4}$	1.757 <sup>c</sup>	
	CC			$4.23 \times 10^{-3}$	2.150	
<b>3a</b>	PP	TD	0.75	$1.52 \times 10^{-4}$	0.887	54.9
	PC			$1.01 \times 10^{-3}$	2.213	
	CC			$5.46 \times 10^{-3}$	1.317	
<b>3a</b>	PP	TD	0.10	$1.36 \times 10^{-4}$	0.711	65.8
	PC		(last)	$9.17 \times 10^{-4}$	1.829	
	CC			$5.51 \times 10^{-3}$	2.215	
<b>2b</b>	PP	mes	0.10	-	-	80.6
	PC			$1.14 \times 10^{-3}$	1.234	
	CC			$8.40 \times 10^{-3}$	1.951	
<b>2c</b>	PP	SQ	0.10	$1.11 \times 10^{-4}$	1.296	45.2
	PC <sup>c</sup>			$5.00 \times 10^{-4}$	1.838 <sup>c</sup>	
	CC			$3.69 \times 10^{-3}$	0.908	
<b>2c</b>	PP	SQ (100°C)	0.10	$1.19 \times 10^{-4}$	0.633	61.9
	PC			$7.35 \times 10^{-4}$	1.645	
	CC			$4.39 \times 10^{-3}$	1.544	
<b>2d</b>	PP	BN	0.10	$1.25 \times 10^{-4}$	1.753	20.6
	PC			$5.55 \times 10^{-4}$	1.187	
	CC			$6.60 \times 10^{-3}$	0.016	
<b>2d</b>	PP	CN	0.10	$1.13 \times 10^{-4}$	0.417	35.5
	PC			$5.49 \times 10^{-4}$	0.525	
	CC			$4.82 \times 10^{-3}$	0.111	
<b>2e</b>	PP	PrC	-0.10	$9.47 \times 10^{-5}$	0.845	22.9
	PC			$3.04 \times 10^{-4}$	0.519	
	CC			$5.25 \times 10^{-3}$	0.068	
<b>2e</b>	PP	PrC	0.10	$1.01 \times 10^{-4}$	1.160	19.4
	PC			$3.00 \times 10^{-4}$	0.497	
	CC			$6.40 \times 10^{-3}$	0.090	

<sup>a</sup> Measurements of  ${}^t\text{Bu}$  typically give three conductance peaks assigned to junctions with PP, PC, or CC geometries. Peak conductance values (G<sub>peak</sub>), and areas, are obtained from Gaussian deconvolution of 1D histograms using MagicPlot (Magicplot Systems, LLC; **Figure S3**). <sup>b</sup> The percentage of chemisorbed contacts (%-C) is calculated using %-C = [(areaCC + areaPC/2) / (total area)] × 100. <sup>c</sup> The width of the Gaussian fit to this peak feature was constrained (such that the conductance values at half the peak maximum were  $10^{G_{peak} \pm 0.45}$  G<sub>0</sub>) to improve the total fit.

**Table S2.** Conductance data from *repeated* measurements of  ${}^6\text{Bu}$  in **Figures S4, S6, and S7**.<sup>a</sup>

panel	geometry	conditions	V <sub>bias</sub> (V)	conductance (G <sub>0</sub> )	absolute area	%-C <sup>b</sup>
<b>S4a</b>	PP	TD, gold-on-steel, 1 h	0.10	$1.11 \times 10^{-4}$	0.602	64.8
	PC			$7.07 \times 10^{-4}$	1.688	
	CC	equilibration		$4.25 \times 10^{-3}$	1.816	
<b>S4b</b>	PP	TD, Au <sup>TS</sup> , frequently recut tip	0.10	$1.12 \times 10^{-4}$	1.640	34.7
	PC <sup>c</sup>			$4.85 \times 10^{-3}$ <sup>c</sup>	1.283	
	CC			$3.75 \times 10^{-3}$	0.571	
<b>S6b</b>	PP	TD	0.10	$1.19 \times 10^{-4}$	0.624	56.9
	PC <sup>c</sup>		(first)	$7.69 \times 10^{-4}$ <sup>c</sup>	1.627 <sup>c</sup>	
	CC			$4.22 \times 10^{-3}$	1.082	
<b>S6b</b>	PP	TD	0.75	$1.46 \times 10^{-4}$	0.607	50.0
	PC			$1.02 \times 10^{-3}$	2.394	
	CC			$5.36 \times 10^{-3}$	0.604	
<b>S6b</b>	PP	TD	0.10	$1.10 \times 10^{-4}$	0.241	56.8
	PC		(last)	$6.18 \times 10^{-4}$	0.932	
	CC			$3.89 \times 10^{-3}$	0.464	
<b>S6c</b>	PP	TD	0.10	$1.22 \times 10^{-4}$	1.036	57.2
	PC			$7.00 \times 10^{-4}$	2.015	
	CC			$4.43 \times 10^{-3}$	1.728	
<b>S6c</b>	PP	TD	0.75	$1.39 \times 10^{-4}$	1.222	39.9
	PC <sup>c</sup>			$7.10 \times 10^{-4}$ <sup>c</sup>	2.196 <sup>c</sup>	
	CC			$4.65 \times 10^{-3}$	0.442	
<b>S6e</b>	PP	SQ	0.10	$1.17 \times 10^{-4}$	1.507	41.9
	PC			$6.19 \times 10^{-4}$	1.926	
	CC			$4.01 \times 10^{-3}$	0.818	
<b>S6e</b>	PP <sup>c</sup>	SQ (100°C)	0.10	$1.70 \times 10^{-4}$ <sup>c</sup>	0.675	65.4
	PC <sup>c</sup>			$6.75 \times 10^{-4}$ <sup>c</sup>	1.601	
	CC			$4.64 \times 10^{-3}$	1.991	
<b>S6f</b>	PP	SQ	0.10	$1.10 \times 10^{-4}$	1.434	37.9
	PC			$5.47 \times 10^{-4}$	1.843	
	CC			$4.13 \times 10^{-3}$	0.518	
<b>S6f</b>	PP <sup>c</sup>	SQ (100°C)	0.10	$1.83 \times 10^{-4}$ <sup>c</sup>	0.684	62.0
	PC <sup>c</sup>			$8.35 \times 10^{-4}$ <sup>c</sup>	1.536	
	CC			$5.00 \times 10^{-3}$	1.601	
<b>S6g</b>	PP	SQ	0.75	$1.37 \times 10^{-4}$	1.249	46.4
	PC <sup>c</sup>			$8.22 \times 10^{-4}$ <sup>c</sup>	1.945 <sup>c</sup>	
	CC			$4.65 \times 10^{-3}$	0.949	
<b>S6g</b>	PP	SQ (100°C)	0.75	$1.85 \times 10^{-4}$	0.448	68.6
	PC			$1.15 \times 10^{-3}$	1.569	
	CC			$5.37 \times 10^{-3}$	1.906	

<b>S6h</b>	PP	mes (2)	0.10	-	-	81.0
	PC <sup>c</sup>			$9.81 \times 10^{-4} \text{ } c$	1.030	
	CC <sup>c</sup>			$7.25 \times 10^{-3} \text{ } c$	1.688	
<b>S6h</b>	PP <sup>c</sup>	mes (3)	0.10	$2.46 \times 10^{-4} \text{ } c$	0.841	55.9
	PC <sup>c</sup>			$1.38 \times 10^{-3} \text{ } c$	1.962	
	CC			$7.12 \times 10^{-3}$	1.328	
<b>S7a</b>	PP	BN (2)	0.10	$1.56 \times 10^{-4}$	1.076	39.7
	PC			$1.08 \times 10^{-3}$	2.128	
	CC			$7.07 \times 10^{-3}$	0.346	
<b>S7a</b>	PP	BN (3)	0.10	$1.36 \times 10^{-4}$	1.063	25.6
	PC			$8.31 \times 10^{-3}$	1.116	
	CC			-	-	
<b>S7a</b>	PP	BN (4)	0.10	$1.38 \times 10^{-4}$	1.206	21.4
	PC			$7.61 \times 10^{-4}$	0.899	
	CC			-	-	
<b>S7b</b>	PP	CN (2)	0.10	$1.77 \times 10^{-4}$	0.665	25.1
	PC <sup>c</sup>			$8.45 \times 10^{-4} \text{ } c$	0.424 <sup>c</sup>	
	CC			$4.44 \times 10^{-3}$	0.081	
<b>S7c</b>	PP	PrC (2)	-0.10	$1.06 \times 10^{-4}$	0.900	18.5
	PC			$5.08 \times 10^{-4}$	0.298	
	CC			$3.90 \times 10^{-3}$	0.090	
<b>S7c</b>	PP	PrC (2)	0.10	$9.73 \times 10^{-5}$	0.981	18.3
	PC			$4.21 \times 10^{-4}$	0.416	
	CC			$3.93 \times 10^{-3}$	0.058	

<sup>a</sup> Measurements of **Bu** typically give three conductance peaks assigned to junctions with PP, PC, or CC geometries. Peak conductance values ( $G_{\text{peak}}$ ), and areas, are obtained from Gaussian deconvolution of 1D histograms using MagicPlot (Magicplot Systems, LLC; **Figure S3**). <sup>b</sup> The percentage of chemisorbed contacts (%-C) is calculated as described in using % - C = [(areaCC + areaPC/2) / (total area)] × 100. <sup>c</sup> The width of the Gaussian fit to this peak feature was constrained (such that the conductance values at half the peak maximum were  $10^{G_{\text{peak}} \pm 0.45} G_0$ ) to improve the total fit.

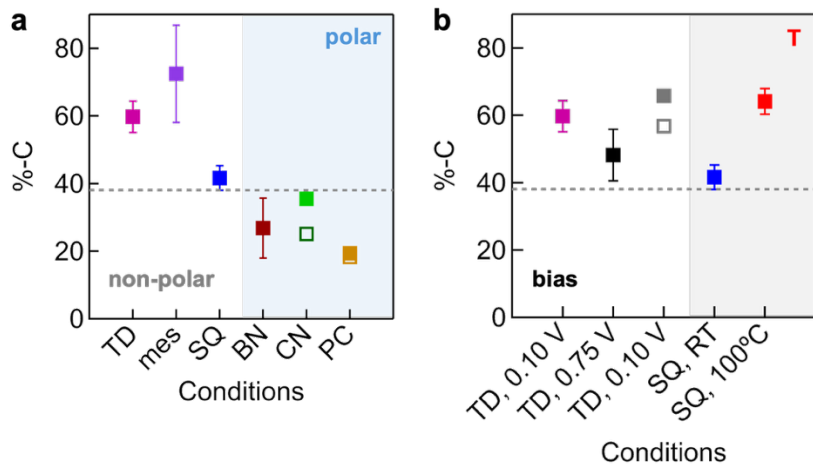


**Figure S2.** Plots of the percentage of chemisorbed contacts (%-C) for '**Bu** (data from **Table S1** and **S2**) measured in different **(a)** non-polar (left) or polar solvents (right, shaded region) or **(b)** at different biases in TD (left) or at different temperatures in SQ (right, shaded region). Solid markers correspond to the average %-C (when >3 measurements were performed, error bars = 1 standard deviation) or the first measurement (corresponding to the datasets presented in **Figures 2** and **3**). The dotted line at %-C = 38% is provided as a guide to the eye, and to separate the “non-polar” and “polar” solvent data. However, we note that solvent dielectric and dipole moment are a continuum and there are likely other solvent properties which may also influence these reactions. Data in **Table S1** and **S2** that is not plotted here corresponds to measurements that have been performed only once with those solvents/conditions.

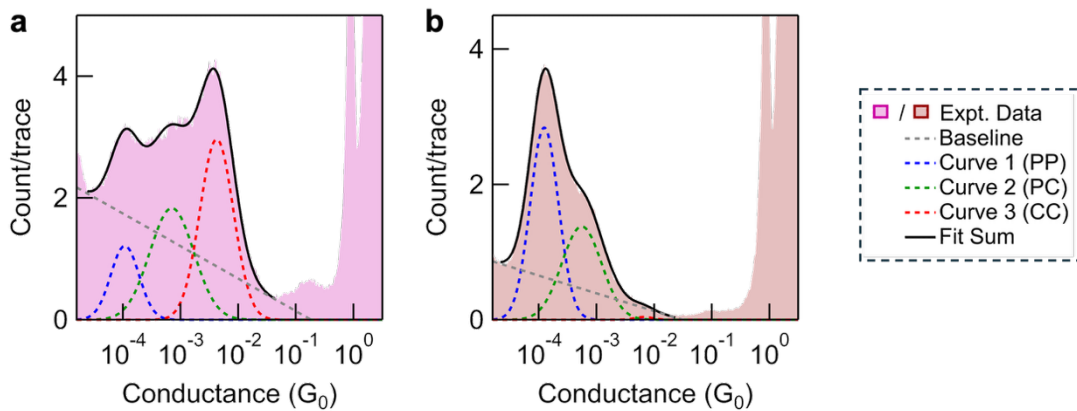


**Figure S3.** Representative fits to conductance histograms obtained from measurements of '**Bu** in **(a)** TD (large %-C) and **(b)** BN (small %-C). These histograms correspond to the datasets presented in **Figure 2b,d**. *Right:* a key to the different figure components (dotted box).

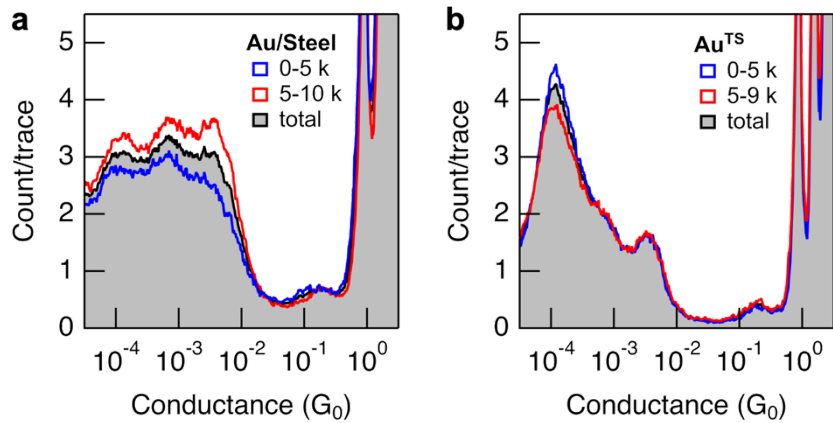


**Figure S4.** 1D conductance histograms for measurements of *'Bu* in TD (0.10 V,  $\geq 9,000$  traces) performed using a: (a) gold-on-steel substrate with the same STM tip, after allowing the system to equilibrate for 1 h to *minimize* tip-substrate drift; (b) template-stripped gold ( $Au^{TS}$ ) substrate, recutting the tip every 1,000 traces to *maximize* tip-substrate drift. The data in panel (a) confirms that we obtain a large %C (= 64.8%) for measurements proximal to a rough gold surface (the initially rough gold-on-steel surface is further roughened locally through repeated break-junction measurements<sup>21</sup>). The data in panel (b) shows that we obtain a small %C (= 34.7%) for measurements proximal to a flat gold surface ( $Au^{TS}$  substrates exhibit ultra-flat surfaces over large areas,<sup>22</sup> any roughness generated by the break-junction measurements is effectively moved away from the junction as the tip drifts in the x-y plane relative to the substrate). Together, these experiments support the hypothesis that such S-C( $sp^3$ ) bond cleavage reactions are observed more frequently when the surface near the junction is rough.

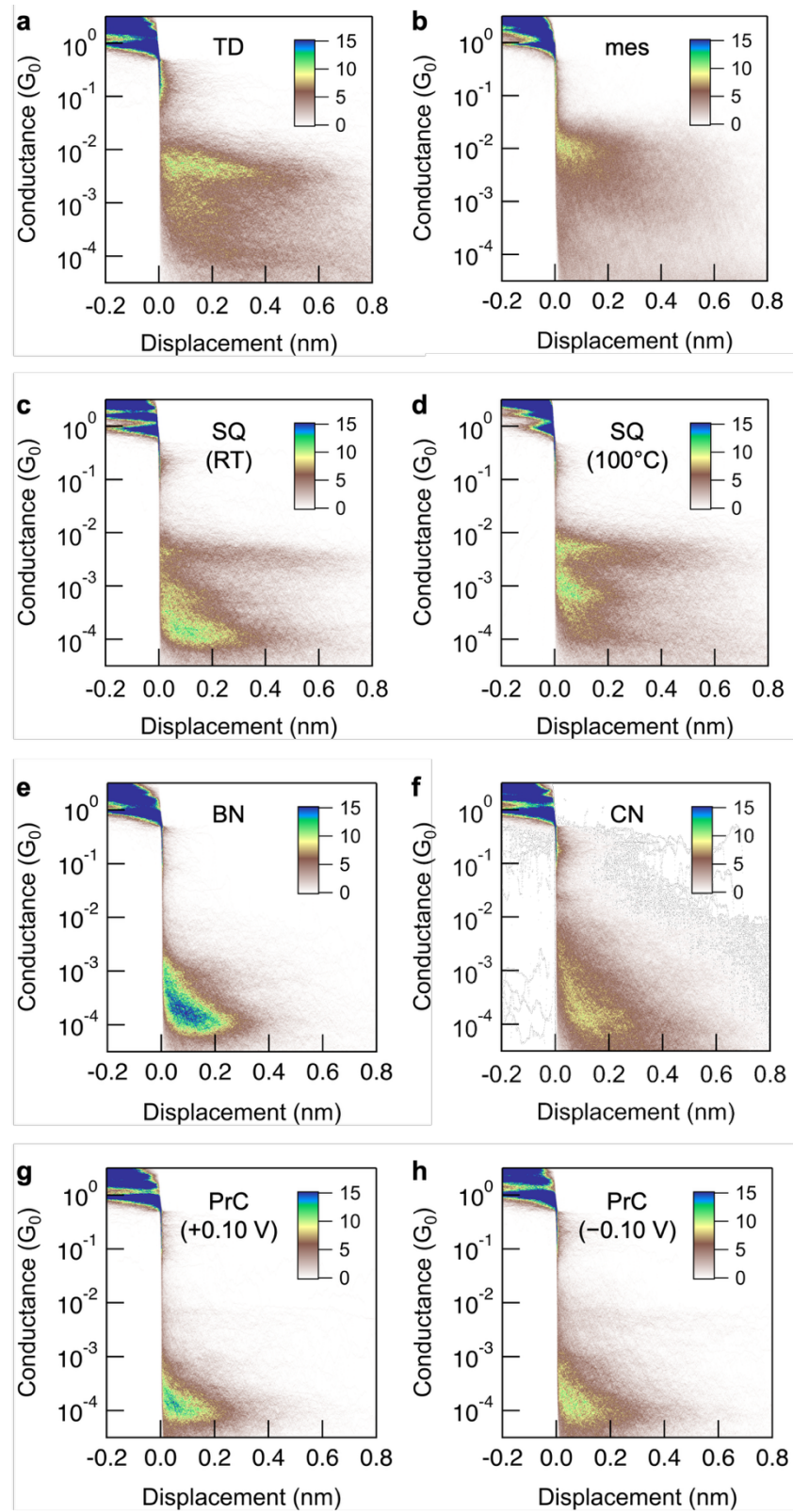


**Figure S5.** 2D conductance-displacement histograms obtained from measurements of **'Bu**, corresponding to the 1D conductance histograms shown in **Figure 2**.

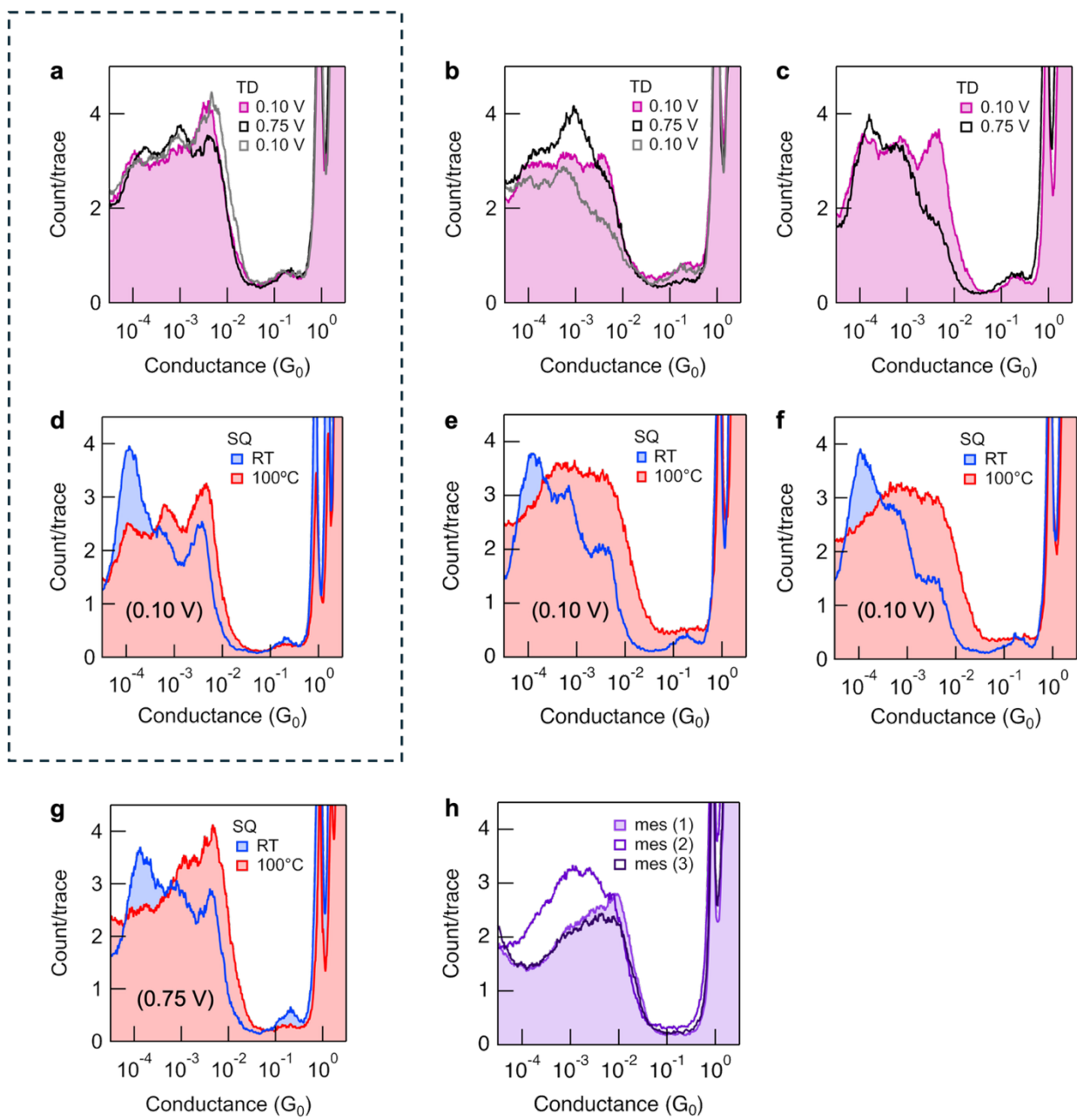


**Figure S6.** Overlaid 1D histograms for repeated measurements of  ${}^t\text{Bu}$  performed in *non-polar* solvents: **(a-c)** TD at different  $V_{\text{bias}}$ ; **(d-g)** SQ at different  $V_{\text{bias}}$  and temperature; **(h)** mes at  $V_{\text{bias}} = 0.1$  V. Boxed panels (a) and (d), and the solid histogram for measurements of  ${}^t\text{Bu}$  in mes (“mes (1)”) are reproduced here from **Figures 2b,c**, and **3a** for convenience. The experiment-to-experiment variation observed between TD measurements (summarized in **Figure S2**) obfuscate the possible influences of applied external electric field and ambient environment on this interfacial S-C( $sp^3$ ) bond cleavage reaction, as discussed in the manuscript.

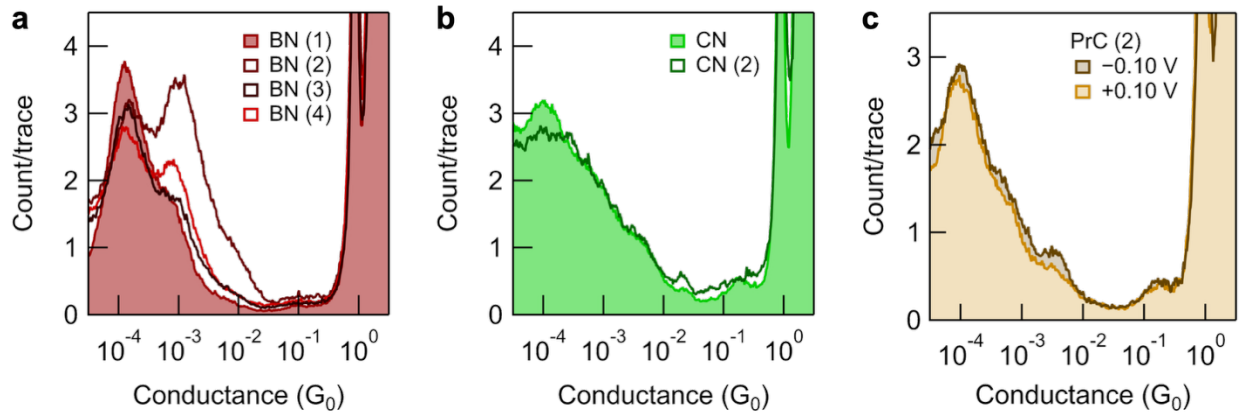


**Figure S7.** Overlaid 1D histograms for repeated measurements of  ${}^t\text{Bu}$  performed in *polar* solvents: **(a)** BN and **(b)** CN at  $V_{bias} = 0.10$  V, and **(c)** PC at  $V_{bias} = \pm 0.10$  V. Solid histograms in panels (a) and (b) are reproduced here from **Figure 2c** for convenience.

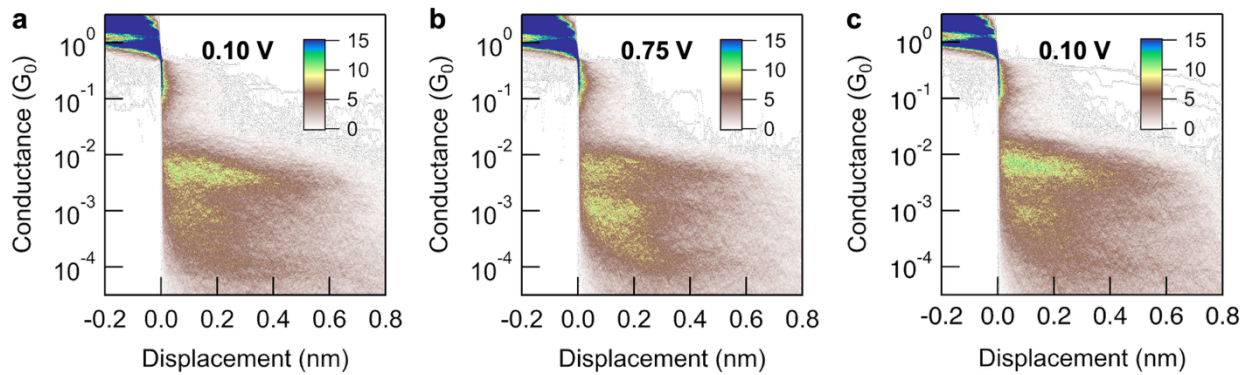


**Figure S8.** 2D conductance-displacement histograms obtained from measurements of  ${}^t\text{Bu}$ , corresponding to the 1D conductance histograms shown in **Figure 3a**. The histogram in panel (a) is reproduced here from **Figure S5a** for convenience.

*Conductance Measurements of Other Compounds*

**Table S3.** Selected conductance data corresponding to **Figures 4, S11c, and S12.**<sup>a</sup>

entry	molecule	solvent <sup>b</sup>	conductance ( $G_0$ ) <sup>c</sup>	log(noise) (a.u.) <sup>d</sup>	junction formation probability (%) <sup>e</sup>
1a	<b>Tr</b>	TCB (1)	$5.29 \times 10^{-3}$	$4.33 \times 10^{-3}$	69
1b		TCB (2)	$5.67 \times 10^{-3}$	$2.81 \times 10^{-3}$	82
2a	<b>C<sub>7</sub>H<sub>7</sub></b>	TCB (1)	$1.13 \times 10^{-2}$	$2.09 \times 10^{-3}$	96
2b		TCB (2)	$8.27 \times 10^{-3}$	$2.63 \times 10^{-3}$	95
3a	<b>Bn</b>	TCB (1)	$8.00 \times 10^{-4}$	$1.30 \times 10^{-2}$	95
3b		TCB (2)	$4.87 \times 10^{-4}$	$1.22 \times 10^{-2}$	92
3c		TD	$4.34 \times 10^{-4}$	-	-
4a	<b>H</b> <sup>f</sup>	TCB (1)	$5.46 \times 10^{-3}$	$3.49 \times 10^{-3}$	97
4b		TCB (2)	$4.10 \times 10^{-3}$	$4.61 \times 10^{-3}$	95
5a	<b>Me</b>	TCB (1)	$1.62 \times 10^{-3}$	$8.83 \times 10^{-3}$	95
5b		TCB (2)	$1.69 \times 10^{-3}$	$9.27 \times 10^{-3}$	91

<sup>a</sup> All data measured at  $V_{bias} = 0.1$  V unless otherwise stated. <sup>b</sup> The numbers in parentheses (where relevant) indicate repeated experiments. These numbers correspond to those given for each 1D histogram in **Figure S13**. <sup>c</sup> Peak conductance values obtained from Gaussian fits to 1D histogram peaks. <sup>d</sup> The average conductance noise obtained from Gaussian fits to noise histograms in **Figure S14**. <sup>e</sup> Estimated junction formation probability, determined as the percentage of conductance-displacement traces containing a step feature (see *Conductance Noise Analysis* section for details of step identification). <sup>f</sup> Conductance data reported in previous work.<sup>1</sup>

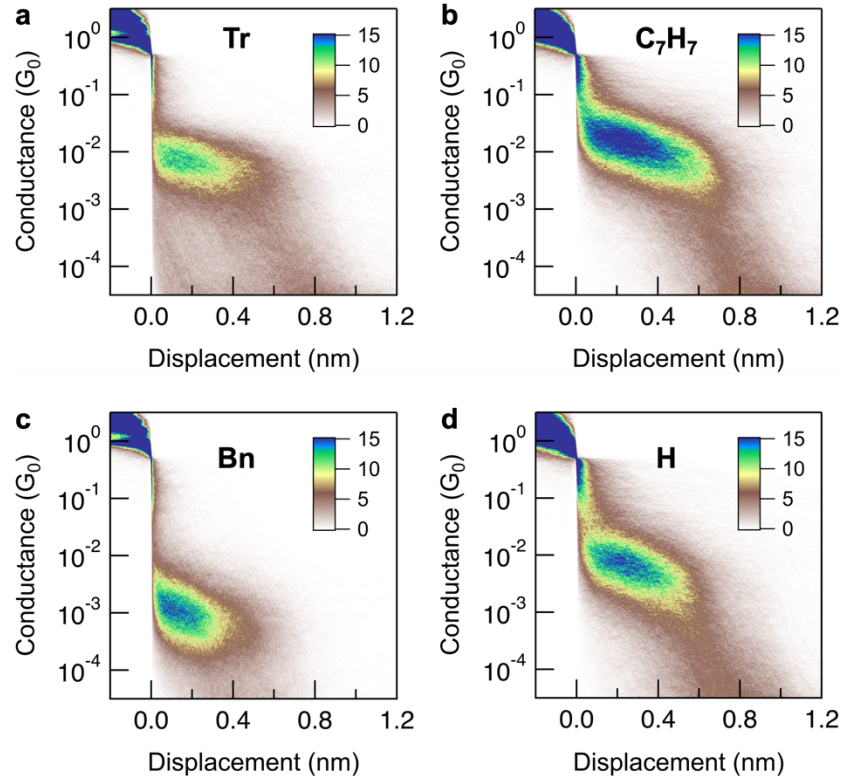


**Figure S9.** 2D conductance-displacement histograms corresponding to the 1D conductance histograms shown in **Figure 4a** for (a) Tr, (b) C<sub>7</sub>H<sub>7</sub>, (c) Bn, (d) H. Data for H in panel (d) is reproduced from [1].

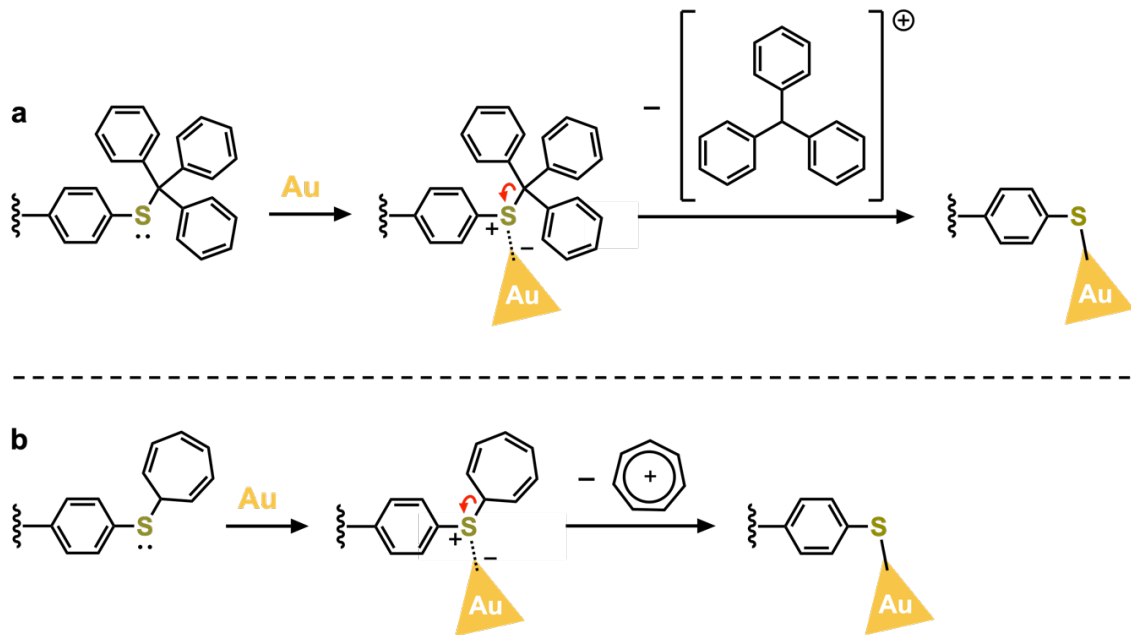


**Figure S10.** Proposed reaction mechanisms for the *in situ* cleavage of (a) tritylium ( $[CPh_3]^+$ ) and (b) tropylium ( $[C_7H_7]^+$ ) carbocations upon coordination of a Lewis basic sulfur group to a Lewis acidic undercoordinated gold adatom.

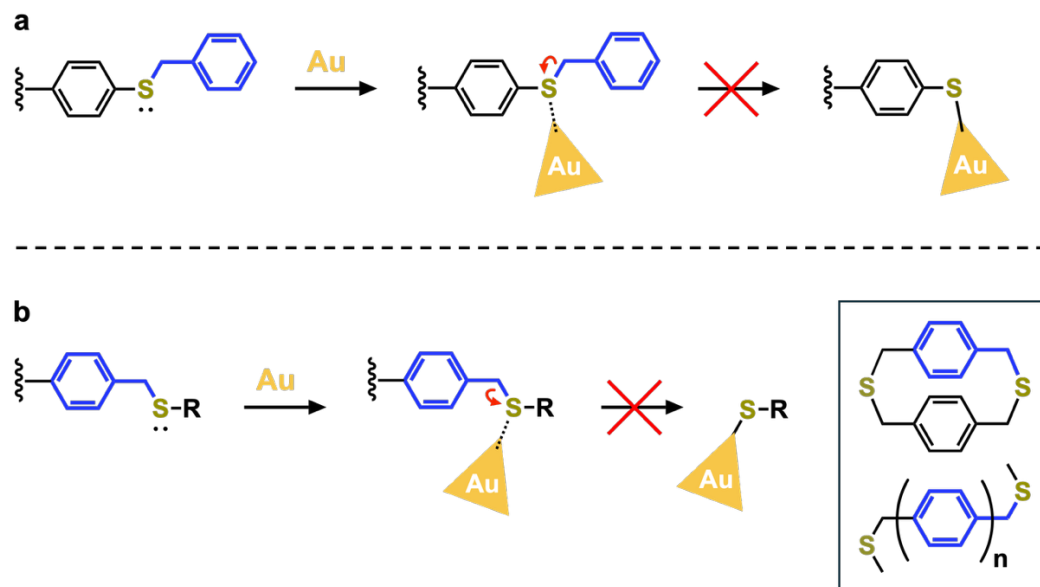


**Figure S11.** Proposed reaction mechanisms for (a) **Bn**, and (b) analogous chemical structures comprising thioether linkers, that are shown here *not* to be feasible under the conditions tested. The similarity between the chemical structure of the  $-S-CH_2-C_6H_5$  contact group of **Bn** and the structures of an analogous  $-C_6H_4-CH_2-SR$  structure are highlighted (bold, blue). These groups have been installed, for example, to form paracyclophane structures that enable studies of constructive quantum interference,<sup>23</sup> or to electronically decouple electrode and molecular backbone states (boxed structures, inset).<sup>24-27</sup>

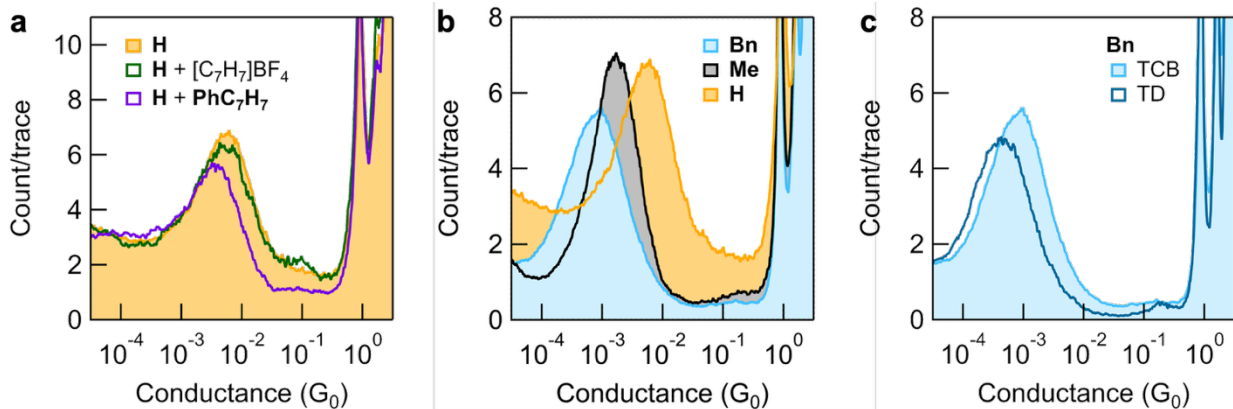


**Figure S12.** (a) Overlaid 1D histograms obtained from measurements of 0.1-0.2 mM solutions of **H** in the absence and presence of two molar equivalents of  $[C_7H_7]BF_4$  or **PhC<sub>7</sub>H<sub>7</sub>** (5,000-10,000 traces,  $V_{bias} = 0.10$  V). These control studies show that the presence of  $[C_7H_7]^+$  – either in bulk solution or generated at the gold surface following coordination of **PhC<sub>7</sub>H<sub>7</sub>** – does not influence the peak intensity or conductance for junctions formed from **H**. Repeated measurements of **H** show experiment to experiment variation of a similar magnitude to the data presented here (Figure S13d). These repeated measurements indicate the small shift to lower conductance, and reduced intensity of the peak in the “**H + PhC<sub>7</sub>H<sub>7</sub>**” histogram is not necessarily attributable to the presence of **PhC<sub>7</sub>H<sub>7</sub>**. (b,c) Overlaid 1D conductance histograms obtained from measurements of **Bn**, **Me**, and **H** in TCB and **Bn** in TCB and TD (5,000-10,000 traces,  $V_{bias} = 0.10$  mV). The lower conductance of **Bn** junctions relative to those formed from **Me** or **H**, even in TD, provides strong evidence that the thioether group remains intact during STM-BJ studies; these junctions exhibit a PP geometry,  $[PhCH_2]^+$  is not cleaved (Figure S11). The filled histograms for **Bn** measurements are reproduced from Figure 4a for convenience. Data for **H** in panels (a) and (b) (filled histograms) are reproduced from [1].

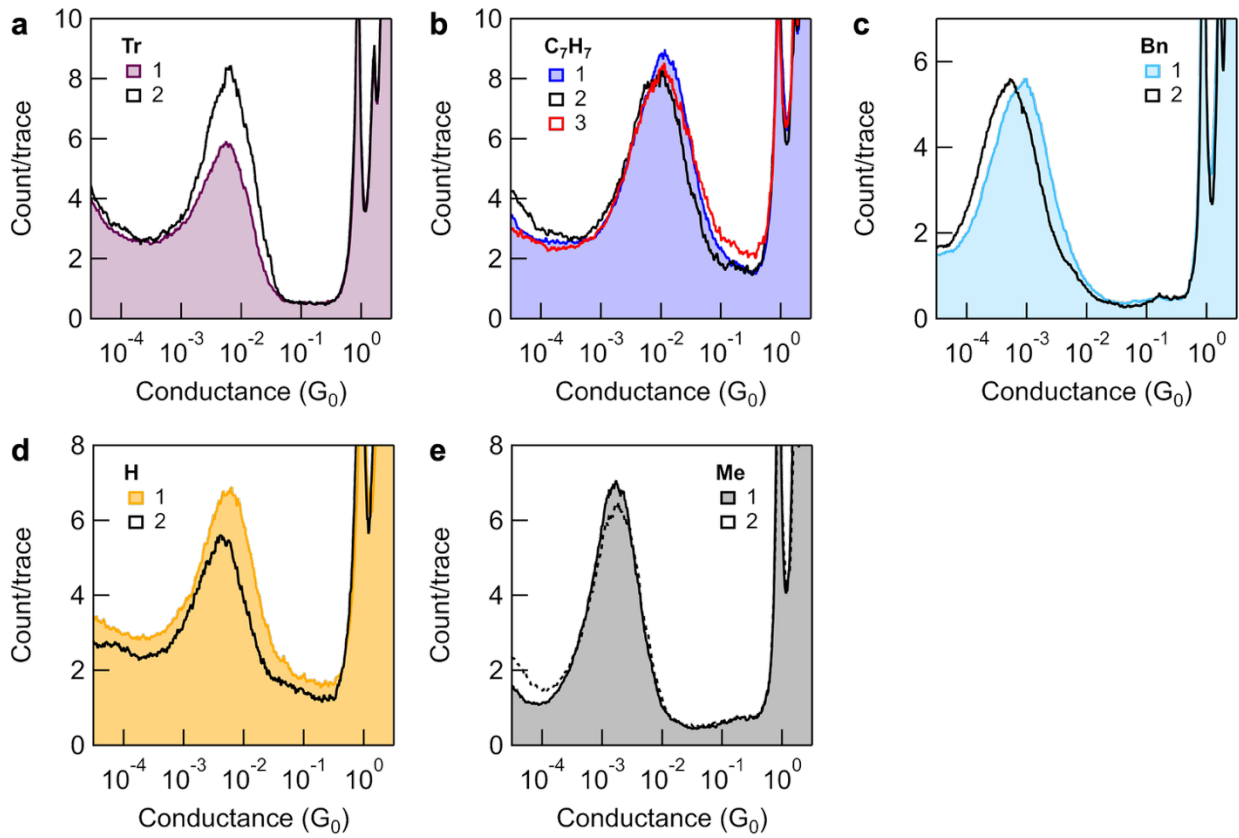


**Figure S13.** Overlaid 1D histograms for repeated measurements of (a) Tr, (b) C<sub>7</sub>H<sub>7</sub>, (c) BN, (d) H, and (e) Me in TCB (5,000-10,000 traces,  $V_{bias} = 0.10$  V). The filled histograms are reproduced here from **Figure 4a** and **Figure S12**, for convenience. Data for H in panel (d) (filled histogram) are reproduced from [1].

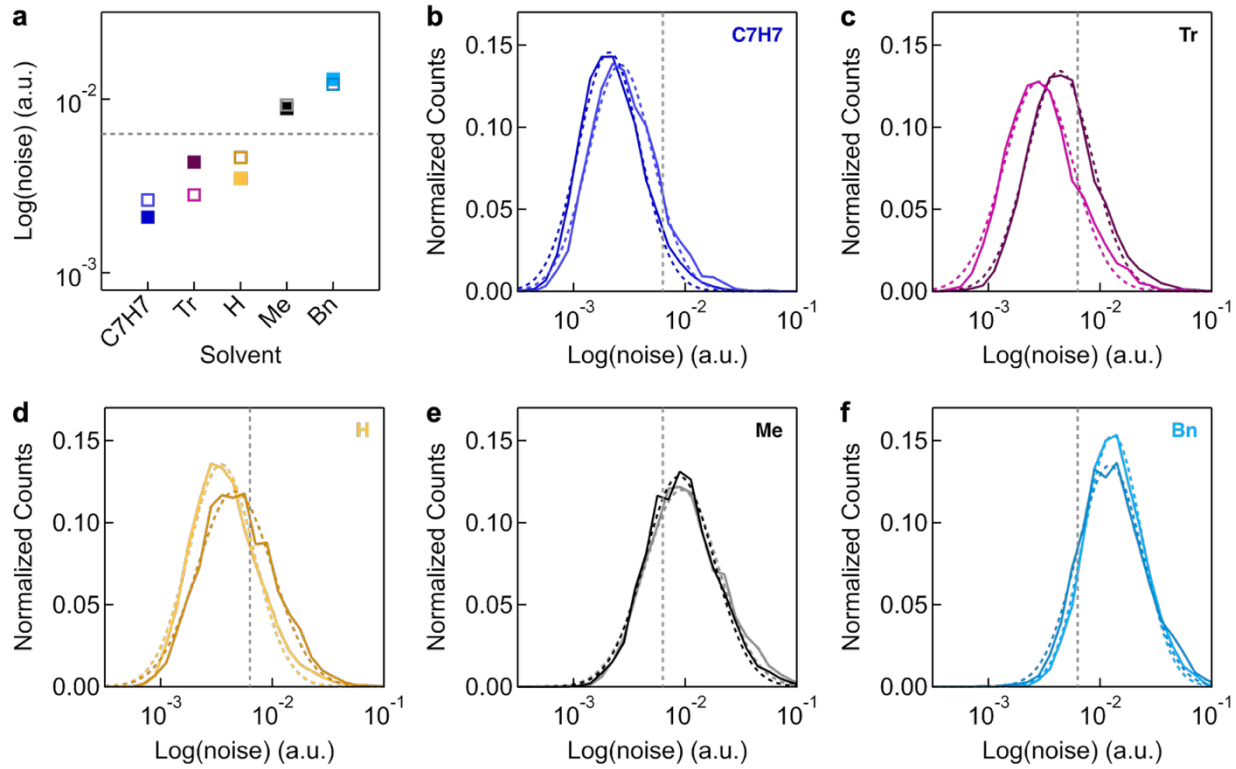


**Figure S14.** (a) A plot of the most probable log(noise) for C<sub>7</sub>H<sub>7</sub>, Tr, H, Me, and Bn junctions, where solid (hollow) markers correspond to the first (second) measurements of each compound. (b-f) Overlaid step noise histograms (solid lines) for each measurement (curved dashed lines are Gaussian fits to each histogram). In all panels, the grey linear dashed lines at  $10^{-2.2}$  are provided as a guide to the eye. Together, this data reveals that junctions formed from H, C<sub>7</sub>H<sub>7</sub>, Tr (junctions assigned as CC geometries) exhibit a smaller step noise compared to junctions formed from Me and Bn (junctions assigned as PP geometries). The results of these analyses align with previous trends in conductance variability observed for junctions with chemisorbed (lower noise) and physisorbed (higher noise) contact chemistries,<sup>5,28,29</sup> corroborating the conclusions proposed here based on the most probable conductance of each junction. Notably, within each of these broad categories (chemisorbed/physisorbed), the step noise also appears to inversely correlate with conductance:  $\text{noise}_{(\text{C}_7\text{H}_7)} < \text{noise}_{(\text{H})}, \text{noise}_{(\text{Tr})}; \text{noise}_{(\text{Me})} < \text{noise}_{(\text{Bn})}$ . Further experimental and computational studies are required to rationalize this finding.

#### 4. Additional Computational Data

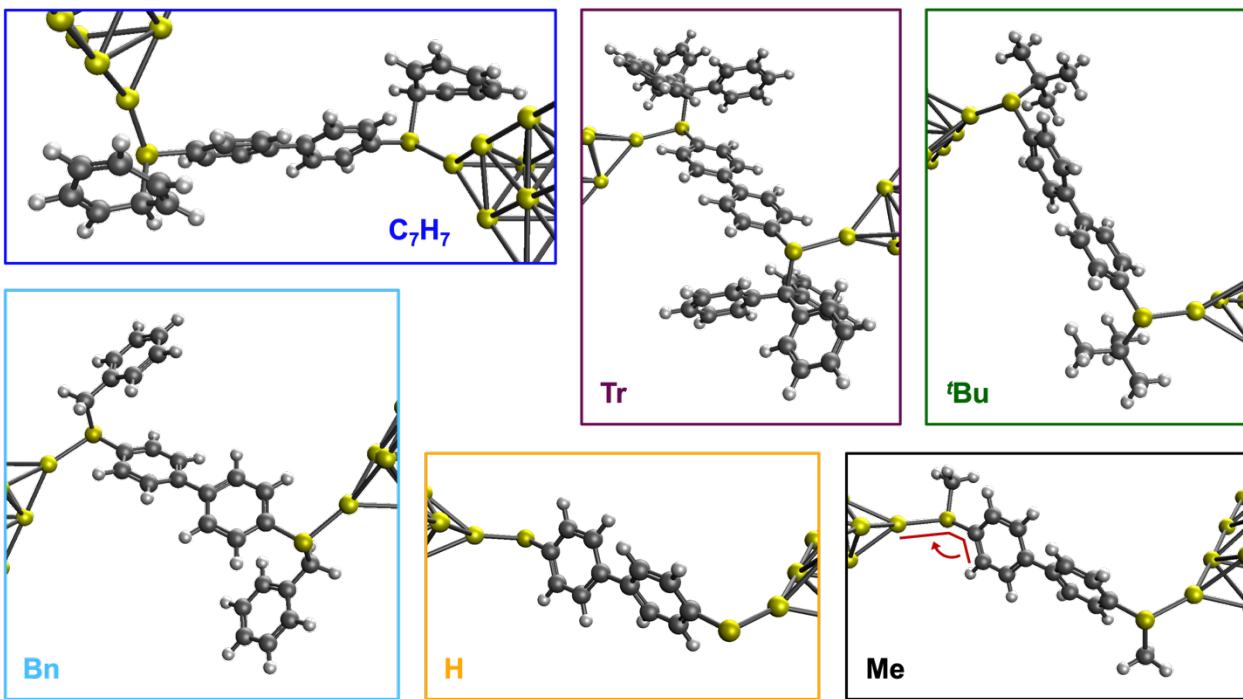


**Figure S15.** Optimized geometries of **C<sub>7</sub>H<sub>7</sub>**, **'Bu**, **Bn**, **H**, and **Me** junctions. For **Tr** junctions, the full geometry of **Tr** is frozen in relaxed configuration obtained for the complex after addition of single gold atoms to each sulfur atom. We found that relaxation of the **Tr** junction after addition of extended gold electrodes resulted in spontaneous S-C bond cleavage to form the tritylium cation. Note that all junctions comprise physisorbed Au-S(R) linkages except for **H** which exhibits a chemisorbed S-Au contact, in line with expectations for solution measurements of thiol-functionalized molecules.<sup>5</sup> The Au-S-C-C dihedral angle is defined for **Me** (red lines), and is calculated for each junction, along with additional structural parameters, in **Table S4**.

**Table S4.** Selected structural parameters for optimized junction geometries.<sup>a</sup>

junction	dihedral angles (°) <sup>b</sup>	avr. deviation from 90 (°) <sup>b</sup>	Au-S (Å)	S-C (Å) <sup>c</sup>
<b>C<sub>7</sub>H<sub>7</sub></b>	130.41, 128.14	39.28	2.3680, 2.3709	2.0765, 2.0269
<b>Tr<sup>d</sup></b>	153.83, 153.83	63.83	2.5060, 2.5060	1.9947, 1.9947
<b>'Bu</b>	141.71, 144.46	53.09	2.4119, 2.4028	1.9031, 1.9048
<b>Bn</b>	143.77, 161.044	62.41	2.4156, 2.4072	1.8702, 1.8765
<b>H</b>	95.73, 81.59	7.07	2.3039, 2.3051	-
<b>Me</b>	98.09, 88.39	4.85	2.4409, 2.4458	1.8208, 1.8183

<sup>a</sup> See **Figure S14** for junction geometries and further discussion. <sup>b</sup> Absolute angles are reported. A dihedral of 90° is close to the optimal value for electronic coupling between the Au-S bind and the conjugated π-orbitals of the backbone.<sup>30</sup> <sup>c</sup> The carbon atom of the thioether substituent, i.e., the methyl group of **Me**. <sup>d</sup> The geometry of **Tr** junctions was not fully optimized (see **Figure S15**).

**Table S5.** Additional computational data for biphenyl-based molecules and junction models.<sup>a</sup>

molecule	HOMO-LUMO gap (eV) <sup>b</sup>	calculated conductance ( $G_0$ ) <sup>c</sup>
<b>C<sub>7</sub>H<sub>7</sub></b>	2.622	$1.02 \times 10^{-4}$
<b>Tr<sup>d</sup></b>	2.751	$3.35 \times 10^{-5}$
<b>'Bu</b>	2.941	$1.85 \times 10^{-4}$
<b>Bn</b>	2.831	$1.54 \times 10^{-4}$
<b>H</b>	3.141	$7.13 \times 10^{-2}$
<b>Me</b>	3.022	$9.60 \times 10^{-3}$

<sup>a</sup> See *Computational Details* section for more information on the methods used. <sup>b</sup> For the gas phase molecule before adding gold electrodes/clusters. <sup>c</sup> The transmission at  $E_F$ , obtained from the DFT-NEGF calculations presented in **Figure 4c**.

## 5. NMR Spectra

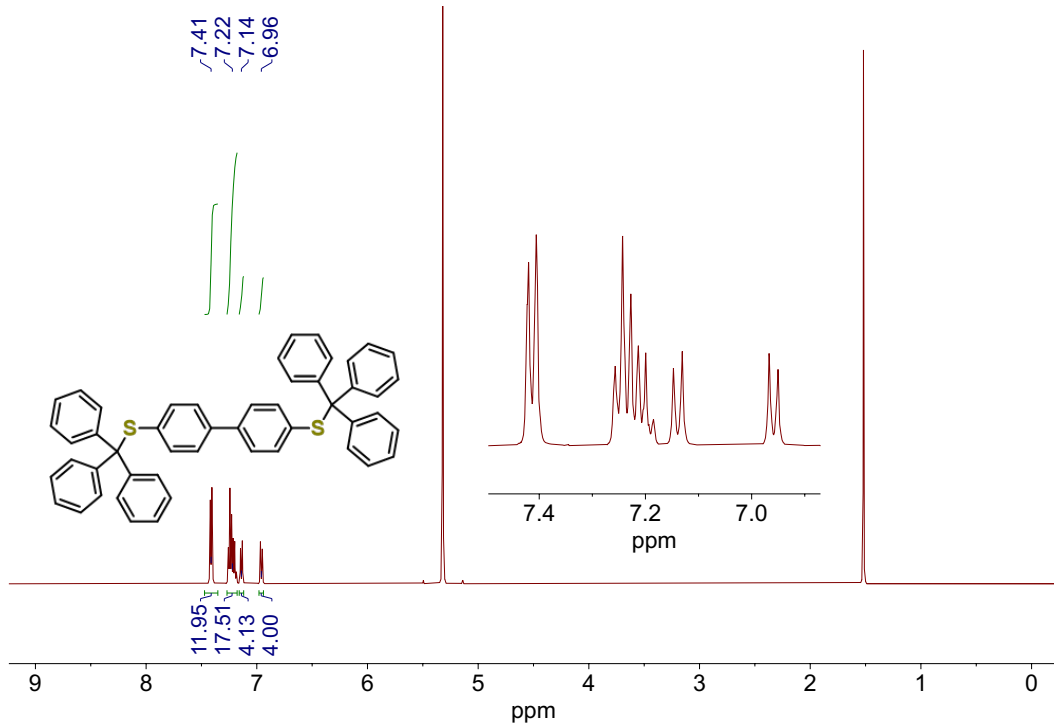


**Figure S16.**  $^1\text{H}$  NMR (500 MHz) spectrum of **Tr** in  $\text{CD}_2\text{Cl}_2$ .

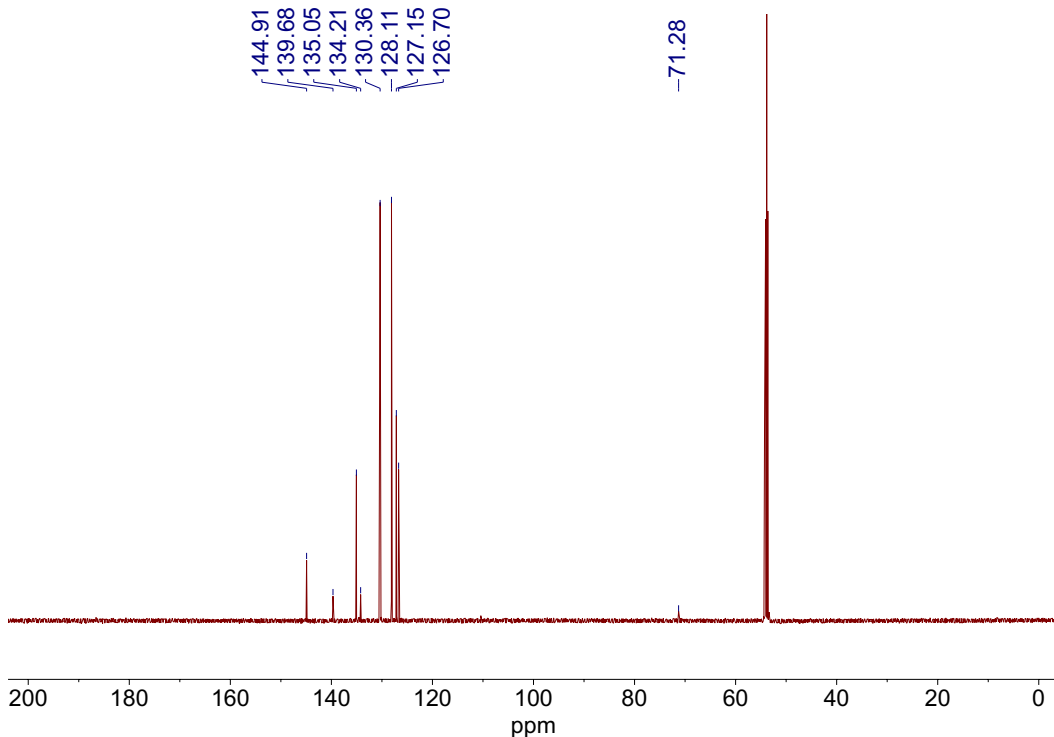


**Figure S17.**  $^{13}\text{C}\{\text{H}\}$  NMR (126 MHz) spectrum of **Tr** in  $\text{CD}_2\text{Cl}_2$ .

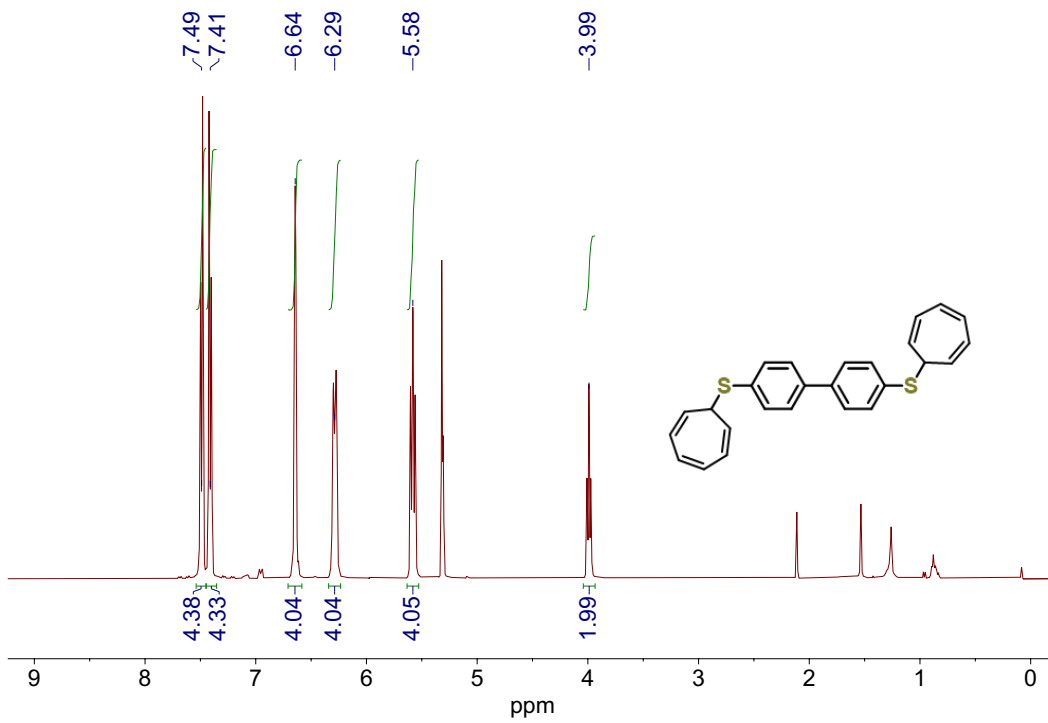


**Figure S18.**  $^1\text{H}$  NMR (400 MHz) spectrum of  $\mathbf{C}_7\mathbf{H}_7$  in  $\text{CD}_2\text{Cl}_2$ .

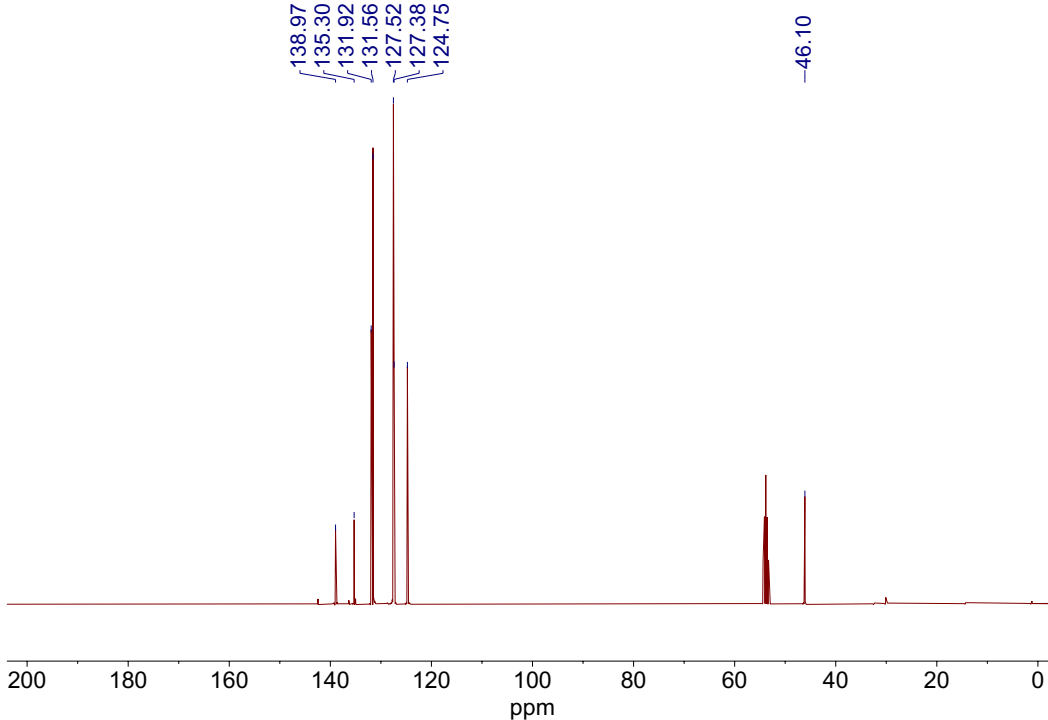


**Figure S19.**  $^{13}\text{C}\{^1\text{H}\}$  NMR (101 MHz) spectrum of  $\mathbf{C}_7\mathbf{H}_7$  in  $\text{CD}_2\text{Cl}_2$ .

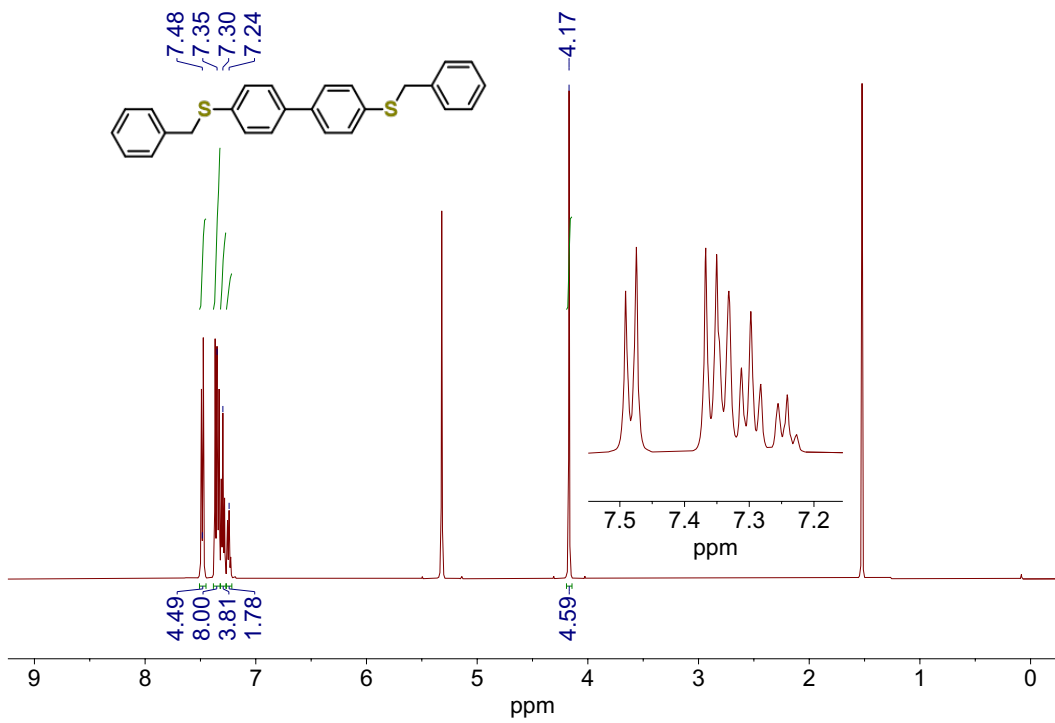


**Figure S20.**  $^1\text{H}$  NMR (500 MHz) spectrum of **Bn** in  $\text{CD}_2\text{Cl}_2$ .

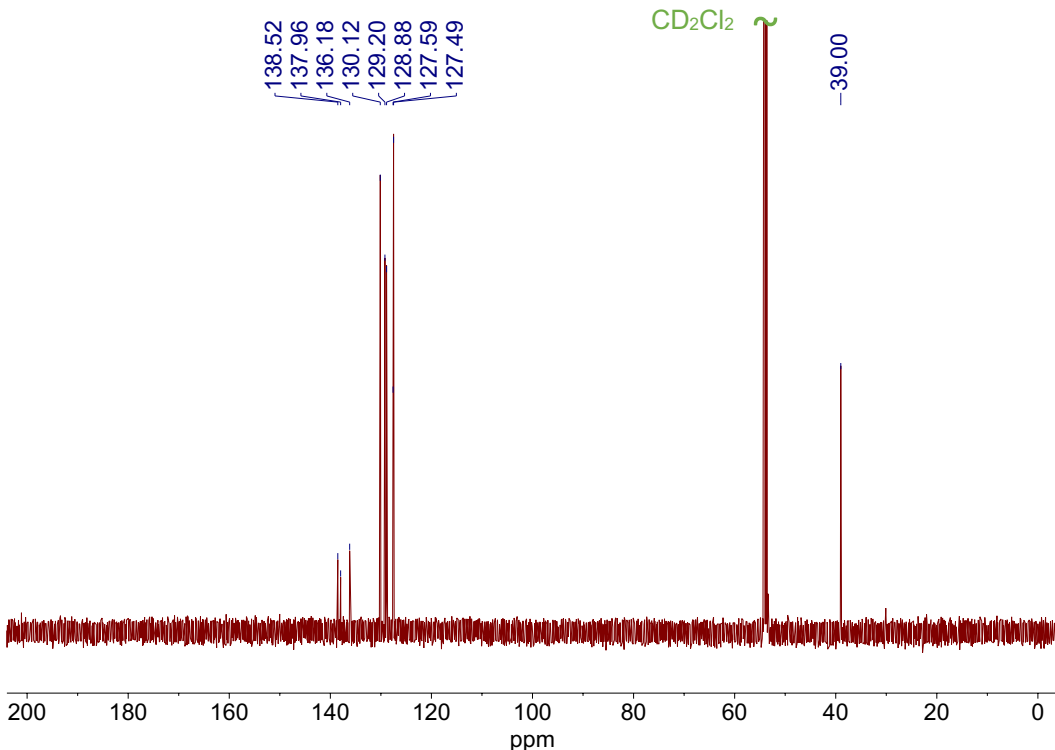


**Figure S21.**  $^{13}\text{C}\{^1\text{H}\}$  NMR (126 MHz) spectrum of **Bn** in  $\text{CD}_2\text{Cl}_2$ .

## 6. References

- (1) Prana, J.; Kim, L.; Czyszczon-Burton, T.; Homann, G.; Chen, S.; Miao, Z.; Camarasa-Gomez, M.; Inkpen, M. Lewis-Acid Mediated Reactivity in Single-Molecule Junctions. *J. Am. Chem. Soc.* **2024**, *146* (48), 33265–33275.
- (2) Fulmer, G. R.; Miller, A. J. M.; Sherden, N. H.; Gottlieb, H. E.; Nudelman, A.; Stoltz, B. M.; Bercaw, J. E.; Goldberg, K. I. NMR Chemical Shifts of Trace Impurities: Common Laboratory Solvents, Organics, and Gases in Deuterated Solvents Relevant to the Organometallic Chemist. *Organometallics* **2010**, *29* (9), 2176–2179.
- (3) Kim, L.; Czyszczon-Burton, T. M.; Nguyen, K. M.; Stukey, S.; Lazar, S.; Prana, J.; Miao, Z.; Park, S.; Chen, S. F.; Inkpen, M. S. Low Vapor Pressure Solvents for Single-Molecule Junction Measurements. *Nano Lett.* **2024**, *24* (32), 9998–10005.
- (4) Venkataraman, L.; Klare, J. E.; Tam, I. W.; Nuckolls, C.; Hybertsen, M. S.; Steigerwald, M. L. Single-Molecule Circuits with Well-Defined Molecular Conductance. *Nano Lett.* **2006**, *6* (3), 458–462.
- (5) Inkpen, M. S.; Liu, Z.; Li, H.; Campos, L. M.; Neaton, J. B.; Venkataraman, L. Non-Chemisorbed Gold–Sulfur Binding Prevails in Self-Assembled Monolayers. *Nature Chem.* **2019**, *11*, 351–358.
- (6) Miao, Z.; Quainoo, T.; Czyszczon-Burton, T. M.; Rotthowe, N.; Parr, J. M.; Liu, Z.; Inkpen, M. S. Charge Transport across Dynamic Covalent Chemical Bridges. *Nano Lett.* **2022**, *22* (20), 8331–8338.
- (7) Nagahara, L. A.; Thundat, T.; Lindsay, S. M. Preparation and Characterization of STM Tips for Electrochemical Studies. *Rev. Sci. Instr.* **1989**, *60* (10), 3128–3130.
- (8) Weiss, E. A.; Kaufman, G. K.; Kriebel, J. K.; Li, Z.; Schalek, R.; Whitesides, G. M. Si/SiO<sub>2</sub>-Templated Formation of Ultraflat Metal Surfaces on Glass, Polymer, and Solder Supports: Their Use as Substrates for Self-Assembled Monolayers. *Langmuir* **2007**, *23* (19), 9686–9694.
- (9) Hegner, M.; Wagner, P.; Semenza, G. Ultralarge Atomically Flat Template-Stripped Au Surfaces for Scanning Probe Microscopy. *Surf. Sci.* **1993**, *291* (1–2), 39–46.
- (10) Williams, D. B. G.; Lawton, M. Drying of Organic Solvents: Quantitative Evaluation of the Efficiency of Several Desiccants. *J. Org. Chem.* **2010**, *75* (24), 8351–8354.
- (11) Blum, V.; Gehrke, R.; Hanke, F.; Havu, P.; Havu, V.; Ren, X.; Reuter, K.; Scheffler, M. Ab Initio Molecular Simulations with Numeric Atom-Centered Orbitals. *Comp. Phys. Commun.* **2009**, *180* (11), 2175–2196.
- (12) Perdew, J. P.; Burke, K.; Ernzerhof, M. Generalized Gradient Approximation Made Simple. *Phys. Rev. Lett.* **1996**, *77* (18), 3865–3868.
- (13) Lenthe, E. V.; Baerends, E. J.; Snijders, J. G. Relativistic Regular Two-Component Hamiltonians. *J. Chem. Phys.* **1993**, *99* (6), 4597–4610.
- (14) Camarasa-Gómez, M.; Hernangómez-Pérez, D.; Wilhelm, J.; Bagrets, A.; Evers, F. Molecular Transport, in J. W. Abbot, C. M. Acosta, A. Akoush, [and 199 others in alphabetical order], Roadmap for Advancements of the FHI-aims Software Package, *arXiv*, Submission Date: 2025-04-30. DOI: 10.48550/arXiv.2505.00125 (accessed 2025-05-12).
- (15) Camarasa-Gómez, M.; Hernangómez-Pérez, D.; Evers, F. Spin–Orbit Torque in Single-Molecule Junctions from Ab Initio. *J. Phys. Chem. Lett.* **2024**, *15* (21), 5747–5753.

- (16) Arnold, A.; Weigend, F.; Evers, F. Quantum Chemistry Calculations for Molecules Coupled to Reservoirs: Formalism, Implementation, and Application to Benzenedithiol. *J. Chem. Phys.* **2007**, *126* (17), 174101.
- (17) Bagrets, A. Spin-Polarized Electron Transport Across Metal–Organic Molecules: A Density Functional Theory Approach. *J. Chem. Theor. Comp.* **2013**, *9* (6), 2801–2815.
- (18) Lichte, D.; Pirkl, N.; Heinrich, G.; Dutta, S.; Goebel, J. F.; Koley, D.; Gooßen, L. J. Palladium-Catalyzed *Para*-C–H Arylation of Anilines with Aromatic Halides. *Angew. Chem. Int. Ed.* **2022**, *61* (47), e202210009.
- (19) Cavazza, M.; Morganti, G.; Pietra, F. Synthesis of (7-(Alkylthio)- and 7-(Arylthio)Cycloheptatriene)Tricarbonyliron and -Hexacarbonyldiiron Complexes. *J. Org. Chem.* **1980**, *45* (10), 2001–2004.
- (20) Kobayashi, K.; Koyama, E.; Kono, C.; Namatame, K.; Nakamura, K.; Furukawa, N. Evidence for Intermolecular Interaction between Sulfonium and Sulfide Sulfur Atoms and Its Application to Synthesis of Cyclic Bis(Disulfide) Dimer. *J. Org. Chem.* **2001**, *66* (6), 2085–2090.
- (21) He, J.; Sankey, O.; Lee, M.; Tao, N.; Li, X.; Lindsay, S. Measuring Single Molecule Conductance with Break Junctions. *Faraday Discuss.* **2006**, *131* (0), 145–154.
- (22) Vogel, N.; Zieleniecki, J.; Köper, I. As Flat as It Gets: Ultrasmooth Surfaces from Template-Stripping Procedures. *Nanoscale* **2012**, *4* (13), 3820–3832.
- (23) Vazquez, H.; Skouta, R.; Schneebeli, S.; Kamenetska, M.; Breslow, R.; Venkataraman, L.; Hybertsen, M. S. Probing the Conductance Superposition Law in Single-Molecule Circuits with Parallel Paths. *Nature Nanotechnol.* **2012**, *7* (10), 663–667.
- (24) Leary, E.; Zotti, L. A.; Miguel, D.; Márquez, I. R.; Palomino-Ruiz, L.; Cuerva, J. M.; Rubio-Bollinger, G.; González, M. T.; Agrait, N. The Role of Oligomeric Gold–Thiolate Units in Single-Molecule Junctions of Thiol-Anchored Molecules. *J. Phys. Chem. C* **2018**, *122* (6), 3211–3218.
- (25) He, J.; Chen, F.; Liddell, P. A.; Andréasson, J.; Straight, S. D.; Gust, D.; Moore, T. A.; Moore, A. L.; Li, J.; Sankey, O. F.; Lindsay, S. M. Switching of a Photochromic Molecule on Gold Electrodes: Single-Molecule Measurements. *Nanotechnology* **2005**, *16* (6), 695–702.
- (26) Bowers, C. M.; Rappoport, D.; Baghbanzadeh, M.; Simeone, F. C.; Liao, K.-C.; Semenov, S. N.; Źaba, T.; Cyganik, P.; Aspuru-Guzik, A.; Whitesides, G. M. Tunneling across SAMs Containing Oligophenyl Groups. *J. Phys. Chem. C* **2016**, *120* (21), 11331–11337.
- (27) Sangtarash, S.; Vezzoli, A.; Sadeghi, H.; Ferri, N.; O’Brien, H. M.; Grace, I.; Bouffier, L.; Higgins, S. J.; Nichols, R. J.; Lambert, C. J. Gateway State-Mediated, Long-Range Tunnelling in Molecular Wires. *Nanoscale* **2018**, *10* (6), 3060–3067.
- (28) Rascón-Ramos, H.; Artés, J. M.; Li, Y.; Hihath, J. Binding Configurations and Intramolecular Strain in Single-Molecule Devices. *Nature Mater.* **2015**, *14*, 517.
- (29) Rashid, U.; Bro-Jørgensen, W.; Harilal, K.; Sreelakshmi, P.; Mondal, R. R.; Chittari Pisharam, V.; Parida, K. N.; Geetharani, K.; Hamill, J. M.; Kaliginedi, V. Chemistry of the Au–Thiol Interface through the Lens of Single-Molecule Flicker Noise Measurements. *J. Am. Chem. Soc.* **2024**, *146* (13), 9063–9073.
- (30) Park, Y. S.; Widawsky, J. R.; Kamenetska, M.; Steigerwald, M. L.; Hybertsen, M. S.; Nuckolls, C.; Venkataraman, L. Frustrated Rotations in Single-Molecule Junctions. *J. Am. Chem. Soc.* **2009**, *131* (31), 10820–10821.